

## Evaluation of Interior Circulation in a High-Resolution Global Ocean Model. Part I: Deep and Bottom Waters

ALEXANDER SEN GUPTA AND MATTHEW H. ENGLAND

*Centre for Environmental Modelling and Prediction, School of Mathematics, University of New South Wales, Sydney, New South Wales, Australia*

(Manuscript received 2 September 2003, in final form 11 June 2004)

### ABSTRACT

Global watermass ventilation pathways and time scales are investigated using an “eddy permitting” ( $1/4^\circ$ ) offline tracer model. Unlike previous Lagrangian trajectory studies, here an offline model based on a complete tracer equation that includes three-dimensional advection and mixing is employed. In doing so, the authors are able to meaningfully simulate chlorofluorocarbon (CFC) uptake and assess model skill against observation. This is the first time an eddy-permitting model has been subjected to such an assessment of interior ocean ventilation. The offline model is forced by seasonally varying prescribed velocity, temperature, and salinity fields of a state-of-the-art ocean general circulation model. A seasonally varying mixed layer parameterization is incorporated to account for the degradation of surface convection processes resulting from the temporal averaging. A series of CFC simulations are assessed against observations to investigate interdecadal-time-scale ventilation using a variety of mixed layer criteria. Simulated tracer inventories and penetration depths are in good agreement with observations, especially for thermocline, mode, and surface waters. Deep water from the Labrador Sea is well represented, forming a distinct deep western boundary current that branches at the equator, although concentrations are lower than observed. The formation of bottom water, which occurs around the Antarctic margin, is also generally too weak, although there is excellent qualitative agreement with observations in the region of the Ross and Weddell Seas. Multicentury ventilation of the outflow of North Atlantic Deep Water and bottom water from the Antarctic Margin are investigated using 1000-yr passive tracer experiments with specified interior source regions. The model captures many of the detailed pathways evident from observations, with much of the discrepancy accounted for by differences between actual and modeled topography. A comparison between model-derived “tracer age” and  $\Delta^{14}\text{C}$  “advection age” provides a semiquantitative assessment of model skill at these longer time scales.

### 1. Introduction

The ocean’s enormous capacity for the uptake and storage of heat and a variety of anthropogenic greenhouse gases means that the transport of surface waters into the ocean interior is of critical importance to climate studies. In particular, it is the rate of this ventilation by density- (thermohaline) driven or wind-driven watermass formation that controls the amount of possible sequestration that may occur and consequently the ocean’s ability to retard climate change. Routinely measured water properties, such as temperature and salinity, are commonly used to provide information regarding watermass formation processes, such as the depth of surface mixing or convection. They also make it possible to reconstruct the history of a given water mass, in particular, the various (surface) source regions that have played a role in its creation. Although an inval-

able tool, this watermass reconstruction cannot provide unambiguous estimates of the ventilation pathways, nor does it hold any information regarding ventilation rates beyond a seasonal time scale as these properties are close to a steady state in the interior.

Water properties associated with some chemical tracers can, however, provide temporal information and give a clearer picture of ventilation pathways. Two approaches are commonly used. Certain transient tracers can “time stamp” the water while at the surface. For example, the atmospheric ratio of dissolved CFC-11 to CFC-12 has varied measurably over the past few decades, and so in conjunction with an estimate of gas solubilities at the surface, this ratio provides an estimate of the data at which the water left the surface mixed layer [although complications arise as (i) the ratio date has become multivalued since atmospheric concentrations have started to decrease and (ii) the mixing of waters with different ratios can lead to an underestimation of age]. Another approach is to use the tracer as a stopwatch. Here, once the tracer becomes separated from the surface mixed layer, its concentration decreases

---

*Corresponding author address:* Alex Sen Gupta, Centre for Environmental Modelling and Prediction, School of Mathematics, University of New South Wales, Sydney, NSW 2052, Australia.  
E-mail: alexg@maths.unsw.edu.au

with time as a result of radioactive decay (e.g., radio-carbon) or through depletion (e.g., oxygen that is consumed through biological activity). England and Maier-Reimer (2001) provide a review of the use of a variety of chemical tracers. Even with these various approaches, a sparsity of measurements, both spatially and temporally, and the difficulty in obtaining synoptic, subsurface observations mean that there still remains much uncertainty regarding ventilation pathways and rates.

In an attempt to make up for this “undersampling,” general circulation models have been employed to fill the gaps. The observed tracer measurements can then be used to help to calibrate the model or to assess the model’s skill at representing ventilation processes. With the time evolution of the tracer field now available, pathways and time scales become immediately apparent. The models, however, have a space and time-scale problem of their own. Most climate studies that require multicentury integrations are resource limited and must generally be integrated at coarse resolutions. This is a severe limitation as much ocean dynamics cannot, in this case, be directly represented: deep convection is thought to take place over horizontal distances of the order of kilometers; ventilation of the interior ocean is generally associated with narrow boundary currents with cores only a few tens of kilometers wide and, in general, the majority of energy transfer in the ocean takes place at the scale of transient eddies, with diameters of tens of kilometers. These scales are well below the size of current coarse-resolution models and, as such, these models rely on various parameterizations of the subgrid-scale physics. Various studies have shown that, even with advanced parameterizations much ocean dynamics remains poorly represented, and the move to eddy-resolving resolutions is a necessary step forward (England and Rahmstorf 1999; Beismann and Redler 2003).

One option for running a model at high resolution while using only relatively modest computational resources is by executing the model in an “offline” mode in which only tracer evolution is prognostic. In this case the simulation of the oceanic transport of tracer requires the combination of two computational tools. The first is the online ocean general circulation model (OGCM), which defines the grid resolution, the speed and direction of ocean currents, and the temperature and salinity distributions (temperature and salinity cannot be included as prognostic variables in the offline simulation as they feed back on the model’s dynamics via density). The second component is the offline tracer dispersion model, which computes the effects of advection and mixing on the tracer using a prescribed source function and the advective fields diagnosed from the online OGCM. Variations on this approach have been used in a number of studies (Stevens and Stevens 1999; Hazell and England 2003; Aumont et al. 1998; Ribbe and Tomczak 1997) and are the basis for the method adopted here.

This study investigates near-global interdecadal to

multicentury ventilation pathways and time scales. A variety of CFC-11 experiments are integrated with different mixed-layer depth criteria and compared to observed World Ocean Circulation Experiment (WOCE) sections. Two further idealized tracer experiments are integrated for deep and bottom water, employing interior source regions to investigate ventilation pathways over multicentury time scales. The goal of this study is two-fold. First we hope to demonstrate that eddy-permitting models can be meaningfully assessed for representation of water-mass formation processes (such studies generally focus on upper-ocean eddy fields for validation purposes). Second, we provide new estimates of century to millennial ventilation pathways of North Atlantic Deep Water (NADW) and Antarctic Bottom Water (AABW) diagnosed from a global model at eddy-permitting resolution. Our offline methodology allows the investigation of time scales well beyond those normally available to fully prognostic versions of high-resolution models.

The rest of this paper is divided into five sections. Section 2 discusses setup of the offline and online models, along with a description of the parameterizations of tracer mixing, mixed layer depth, and CFC uptake used in the experiments described in section 2c. Section 3 looks at the model’s ability to accurately simulate observed CFC distributions, through a comparison with observations. Section 4 looks at the ventilation pathways inferred by the idealized passive tracer experiments, and section 5 covers the discussion.

## 2. Model description and experimental design

### a. Online ocean general circulation model

The velocity fields used to determine the advective transport of the tracers together with the temperature and salinity fields used to determine density distributions are obtained from the Parallel Ocean Climate Model (POCM), the basic formulation of which is described by Semtner and Chervin (1992), Stammer et al. (1996), and Tokmakian and Challenor (1999). The algorithms used to simulate ocean dynamics are adapted from the Geophysical Fluid Dynamics Laboratory (GFDL) Modular Ocean Model (Bryan 1969; Cox 1984; Pacanowski et al. 1991). The current version (POCM<sub>4C</sub>) simulates ocean circulation in the latitudinal domain from 68°N to 75°S, excluding the Arctic Ocean (to avoid grid convergence problems) on a Mercator grid with latitude–longitude resolution of  $0.4^\circ \cos\phi \times 0.4^\circ$ , ( $\phi$  is latitude), resulting in an average grid size of  $0.25^\circ$  in latitude. The simulation period is 1979 to 1998. Surface forcing of the POCM<sub>4C</sub> consists of 20 years of daily varying momentum, heat and freshwater fluxes from the European Centre for Medium-Range Weather Forecasts (ECMWF) model reanalysis (1979–93) followed by operational fields from the ECMWF (1994–98) (Tokmakian and Challenor 1999). To avoid possible model drift,

corrections to the surface heat and freshwater fluxes in the form of a relaxation to Levitus et al. (1994) monthly surface temperature and salinity are made, with a relaxation time scale of 30 days. In addition a high latitude relaxation to Levitus (1982) temperature and salinity (with a relaxation time scale of 120 days) is made north of 58°N and south of 68°S in the top 2000 m. This is implemented to account for exchange of water properties with areas outside the model domain. These high latitude areas are important regions in which much of the formation of deep and bottom waters occurs. By including temperature–salinity ( $T$ – $S$ ) restoration in the interior at high latitudes, the POCM may suppress vertical convection in the “sponge” layers (Toggweiler et al. 1989). It will, however, ensure correct interior density fields at the northern and southern boundaries of the model, which will force a significant component of the simulated thermohaline circulation.

The model has 20 geopotential depth levels, ranging in thickness from 25 m in the top 100 m to 400 m at the bottom (5500 m). Horizontal mixing of tracers is parameterized using a biharmonic scheme with a mixing coefficient,  $B_h = 5 \times 10^{19} \cos^{2.25} \phi$  (McClean et al. 1997). Vertical mixing uses the scheme of Pacanowski and Philander (1981). For the offline model, 12 mean monthly advection and density fields were calculated by averaging from year 1992 to 1998 of the POCM4C integration.

#### b. Offline tracer model

Our offline tracer model is an adaption of the tracer component of the original GFDL Modular Ocean Model (MOM1) (Bryan 1969; Cox 1984; Pacanowski et al. 1991; Hazell and England 2003). This model is a three-dimensional primitive equation ocean model designed as a flexible tool for ocean and coupled climate modeling. Advection and mixing of tracer within the model is described by the tracer conservation equation:

$$\frac{\partial C}{\partial t} + \mathbf{u} \cdot \nabla C = C_s + (A_v \cdot C_z)_z + \nabla \cdot (A_h \nabla C) + B_h \cdot \nabla^4 C + \Delta C_{\text{MLD}}, \quad (1)$$

where  $\mathbf{u} = (u, v, w)$  is the three-dimensional velocity,  $C$  is the tracer concentration,  $C_s$  is the tracer source,  $A_v$  and  $A_h$  are vertical and horizontal Laplacian mixing coefficients, respectively,  $B_h$  is a horizontal biharmonic mixing coefficient, and  $\Delta C_{\text{MLD}}$  denotes changes in  $C$  due to the parameterization of the mixed layer. This tracer conservation equation therefore relates any change in the concentration of the tracer to changes due to the three components of advection, various mixing terms, and any source terms. The horizontal components of velocity ( $u, v$ ) are obtained from the POCM for each grid box based on monthly averages. The vertical component of velocity is determined diagnostically by continuity.

The POCM resolves ocean dynamical processes at the mesoscale (tens of kilometers) and above (e.g., gyres, western boundary currents, deep ocean jets). This degree of resolution permits a certain amount of eddy mixing in prognostic mode. However, the aliasing resulting from the temporal averaging of ( $u, v$ ) will significantly reduce any offline eddy mixing. This is compounded by the fact that the POCM eddy activity is, in itself, too weak (McClean et al. 1997; Tokmakian and Challenor 1999). Regions that experience high levels of eddy activity, such as western boundary currents (WBC) and the Antarctic Circumpolar Current (ACC), should have higher levels of lateral mixing. There are several methods for indexing the horizontal mixing coefficient as a function of local density gradients and mixing scale lengths (Rix and Willebrand 1996; Visbeck et al. 1997); however, these are yet to be incorporated into this tracer model. Here we restrict horizontal mixing to a weak background Laplacian mixing and a biharmonic mixing parameterization that falls off with latitude, matching the POCM scheme.

Averaging of the prescribed temperature and salinity and thus the density fields caused unreliable results for the Pacanowski and Philander (1981) vertical mixing scheme used by the POCM, when implemented in the offline mode. As a result, vertical mixing has been configured based upon the Bryan and Lewis (1979) scheme that approximates mixing to be a simple function of depth. This scheme is still used widely in ocean and climate model simulations (e.g., Manabe and Stouffer 1996; Hirst et al. 2000). Mixing rates, based upon direct estimates of vertical mixing in the ocean, vary from 0.3 cm s<sup>−1</sup> in the upper ocean, where strong density stratification inhibits vertical motion, to 1.3 cm s<sup>−1</sup> at depth. For the purposes of our offline model this scheme has been slightly modified, with enhanced mixing coefficients of 1 and 0.8 cm s<sup>−1</sup> specified between levels 1 and 2 and between levels 2 and 3, respectively, to account for increased surface wind mixing over the upper 50 m.

#### 1) MIXED LAYER DEPTH (MLD)

Any convective mixing that would have occurred as a result of an unstable water column in the prognostic model would be “mixed out” by the time the temperature and salinity fields are incorporated into the offline tracer model. In addition, the monthly averaging of these fields mean that MLDs would not reach the significant depths attained by sporadic and transient convective overturning. To remedy this, a mixed layer parameterization was implemented. Kara et al. (2000) describe an optimal method for calculating MLD based on a density criterion having a fixed temperature difference and variable salinity; that is, MLD is the depth at which density,  $\sigma_t$ , relative to a near-surface value at some reference depth changes by  $\Delta \sigma_t = \sigma_t(T + \Delta T, S, P) - \sigma_t(T, S, P)$ , where  $T$  is the reference temperature,  $S$  is salinity,

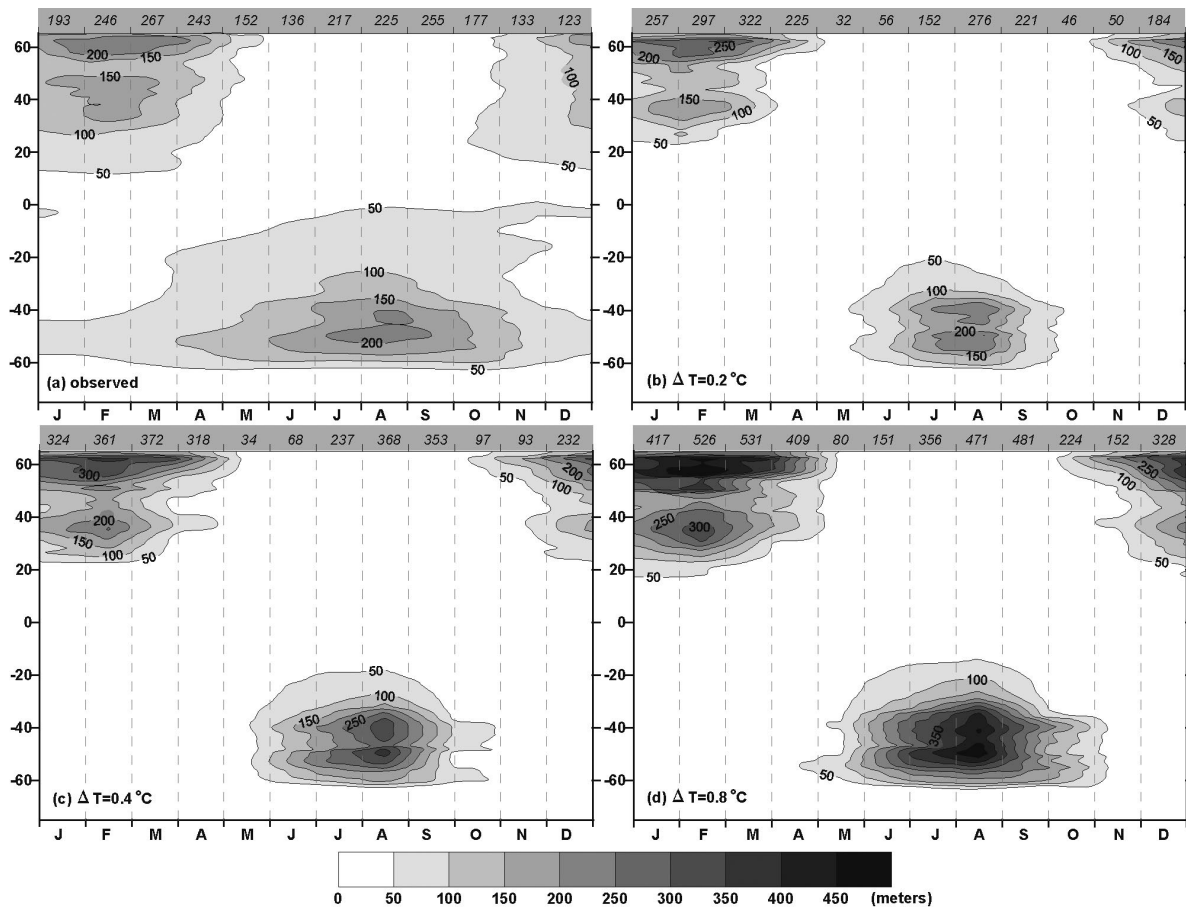


FIG. 1. Monthly Hovmöller plot of zonally averaged mixed layer depths: (a) observed (Kara et al. 2003), (b) CFC<sub>0.2</sub>, (c) CFC<sub>0.4</sub>, and (d) CFC<sub>0.8</sub>. Italicized numbers at the top of each plot represent the maximum zonally averaged MLD (m) each month.

and the pressure  $P = 0$ . Kara et al. (2000) use a reference depth of 10 m; in our model study we use the surface model level (which is centered at 12.5 m);  $\Delta T$  is a constant temperature difference that is optimized by the authors to give the best possible agreement between the *World Ocean Atlas* (Levitus et al. 1994) dataset and a high-resolution climatological time series from the northeastern Pacific Ocean. The resulting optimal temperature difference that they find for this region is  $\Delta T = 0.8^\circ\text{C}$ .

Preliminary results using POCM  $T$  and  $S$  showed that the  $\Delta T = 0.8^\circ\text{C}$  criteria results in maximum MLDs significantly greater than those estimated by Kara et al. (2003) for the global ocean (see Figs. 1a,d). As a result, two other criteria  $\Delta T = 0.2^\circ$  and  $\Delta T = 0.4^\circ\text{C}$  were implemented (Figs. 1b,c). Best agreement for maximum monthly mixed layer depths was evident with the former criteria and, as such,  $\Delta T = 0.2^\circ\text{C}$  was chosen for the long integration idealized tracer experiments (see section 2c). The 12 monthly averaged “convection masks” are calculated prior to the model integrations as a further computational saving. The use of a seasonally varying MLD parameterization represents an important im-

provement over previous offline studies (Ribbe and Tomczak 1997; Stevens and Stevens 1999), which use annually averaged schemes and a result underestimate the depth of convective mixing

## 2) UPTAKE OF CFCs

The air–sea fluxes for the CFC experiments were set up following experiment CF4 of England et al. (1994). Atmospheric CFC-11 concentrations were taken from measurements by Prinn et al. (2000) who give yearly Northern and Southern Hemisphere concentrations between 1930 and 1999. Atmospheric concentrations were interpolated to monthly values in order to match the offline model forcing and a smoothing function was applied between  $30^\circ\text{N}$  and  $30^\circ\text{S}$ . CFC solubility,  $\alpha$ , was calculated using POCM temperature and salinity values in the empirically derived formula of Warner and Weiss (1985). The air–sea flux,  $Q_{\text{CFC}}$ , is proportional to the difference between the saturation concentration  $\alpha C_{\text{atm}}$  and the actual surface water concentration  $C_w$ , namely,

$$Q_{\text{CFC}} = k(\alpha C_{\text{atm}} - C_w). \quad (2)$$



The value for the gas transfer speed  $k$  was taken from the empirical formulation of Wanninkhof (1992), who suggests a dependence of  $k$  on the steady wind speed ( $U$ ) squared. We also reduce  $Q_{\text{CFC}}$  in proportion to the sea ice cover  $R$ , which is assigned a value between 0 and 1 depending on the mean ice coverage at a given point. The exact formulation of  $k$  is then

$$k = 0.31U^2 \left( \frac{\text{Sc}}{660} \right)^{-1/2} (1 - R), \quad (3)$$

where  $\text{Sc}$  is the temperature-dependent Schmidt number (Wanninkhof 1992). The wind dataset was taken from the mean monthly climatology of Esbenson and Kushnir (1981). The ice coverage data were taken from the recent 1° climatology of Reynolds et al. (2001) and 12 monthly means were calculated from the 18 years of observational data. Both ice and wind datasets were interpolated onto the offline model grid using nearest-neighbor and linear interpolation methods, respectively.

### c. Tracer experiments

A series of four CFC-11 experiments,  $\text{CFC}_0$ ,  $\text{CFC}_{0.2}$ ,  $\text{CFC}_{0.4}$ , and  $\text{CFC}_{0.8}$  were integrated with surface CFC-11 concentrations calculated by the method described above, with no parameterized mixed layer ( $\text{CFC}_0$ ) and mixed layers based on a  $\Delta T = 0.2^\circ$ ,  $\Delta T = 0.4^\circ$ , and  $\Delta T = 0.8^\circ\text{C}$  criteria, respectively [see section 2b(2)]. All experiments were integrated from 1935 to 1999 using the atmospheric CFC-11 concentrations of Prinn et al. (2000)].

Experiments in which the tracer source is removed from the surface and is instead released from prescribed interior regions no longer provide an absolute indication of surface ventilation time scales [such an approach was used by Hirst (1999)]. They do, however, provide a useful tool for examining interior ventilation pathways independent of the representation of deep-water formation processes (such as open-ocean convection and downslope flows). Stronger deep tracer signals also make pathways easier to identify. Two 1000-yr passive-tracer integrations were carried out in this regard. The passive tracer is only altered via the model's advection and mixing processes, with no decay term, thereby tracking source water ventilation in the model interior. In the first ( $C_{\text{NADW}}$ ), 100% passive tracer is set in the North Atlantic Ocean north of  $50^\circ\text{N}$  between  $70^\circ\text{W}$  and  $30^\circ\text{E}$  at depths greater than 985 m. In the second ( $C_{\text{BW}}$ ), 100% passive tracer is set in four Antarctic regions at depths greater than 2750 m (the Weddell Sea south of  $65^\circ\text{S}$  between  $65^\circ$  and  $10^\circ\text{W}$ ; the Ross Sea between  $160^\circ\text{E}$  and  $160^\circ\text{W}$ , and south of  $70^\circ\text{S}$ ; Amery Region and south of  $60^\circ\text{S}$  between  $60^\circ$  and  $90^\circ\text{E}$ ; and the Adelie Region south of  $60^\circ\text{S}$  between  $140^\circ$  and  $150^\circ\text{E}$ ). Both experiments,  $C_{\text{NADW}}$  and  $C_{\text{BW}}$  used MLD criteria equivalent to the  $\text{CFC}_{0.2}$  experiment. (Additional animated

sequences from the tracer experiments are available online at [www.maths.unsw.edu.au/~alexg/](http://www.maths.unsw.edu.au/~alexg/).)

## 3. Results from CFC experiments

Dutay et al. (2002) compare the ability of 13 models participating in the Ocean Carbon Intercomparison Project (OCMIP) to reproduce observations of CFC-11 distributions measured during WOCE. Various observed and model sections were compared using depth integrated CFC-11 inventories. A quantitative measure for comparing the mean depth of penetration is also used. This is defined as the depth-integrated inventory divided by the surface concentration at each horizontal position. These provide a useful standard set of tests by which to compare the models.

### a. North Atlantic

NADW originates primarily from two regions: 1) the Labrador Sea, which exports Labrador Sea Water (LSW) formed through open-ocean deep winter convection, and 2) across the Greenland–Iceland–Scotland Ridge, which exports Iceland–Scotland overflow water and Denmark Strait overflow water into the North Atlantic. The export of NADW southward is via a double-cored deep western boundary current (DWBC) that follows the continental shelf of eastern America. The upper core is made up of the less dense Labrador Sea waters, while the lower core is sourced by the overflow waters.

Figure 2a shows CFC-11 values from the National Oceanic and Atmospheric Administration's Eastern North Atlantic section (July–August 1993) nominally along  $20^\circ\text{W}$  extending from  $5^\circ\text{S}$  to Iceland (Castle et al. 1998), hereinafter referred to as NA20W (as per Dutay et al. 2002). A fairly homogeneous CFC layer corresponds to mode water at  $\sim 38^\circ\text{--}45^\circ\text{N}$  centered at  $\sim 500\text{-m}$  depth. This is formed through deep convection and makes up much of the water between the seasonal thermocline and the main thermocline at about 600 m (Doney and Bullister 1992). Between  $15^\circ$  and  $20^\circ\text{N}$  a persistent front is evident at the southern edge of the subtropical gyre where low concentration South Atlantic Central Water (SACW) advected from upwelling regions to the east abuts more recently ventilated North Atlantic Central Water (NACW) (Stramma and Siedler 1988; Kawase and Sarmiento 1985). At greater depths a high CFC signal of LSW can be seen extending south beyond  $\sim 40^\circ\text{N}$  centered just below 1500 m. The only evidence of the denser overflow waters along the NA20W section is within the lower Iceland Basin (near  $55^\circ\text{--}60^\circ\text{N}$ ). In the equatorial region a subsurface maximum is evident between 1500 and 2000 m with a weaker maximum visible between 3500 and 4000 m. Both cores are displaced between  $2^\circ$  and  $5^\circ$  south of the equator. Hydrographic and tracer studies have shown that these cores are a result of eastward advection of the DWBC within extra-equatorial jets (EEJs). These jets

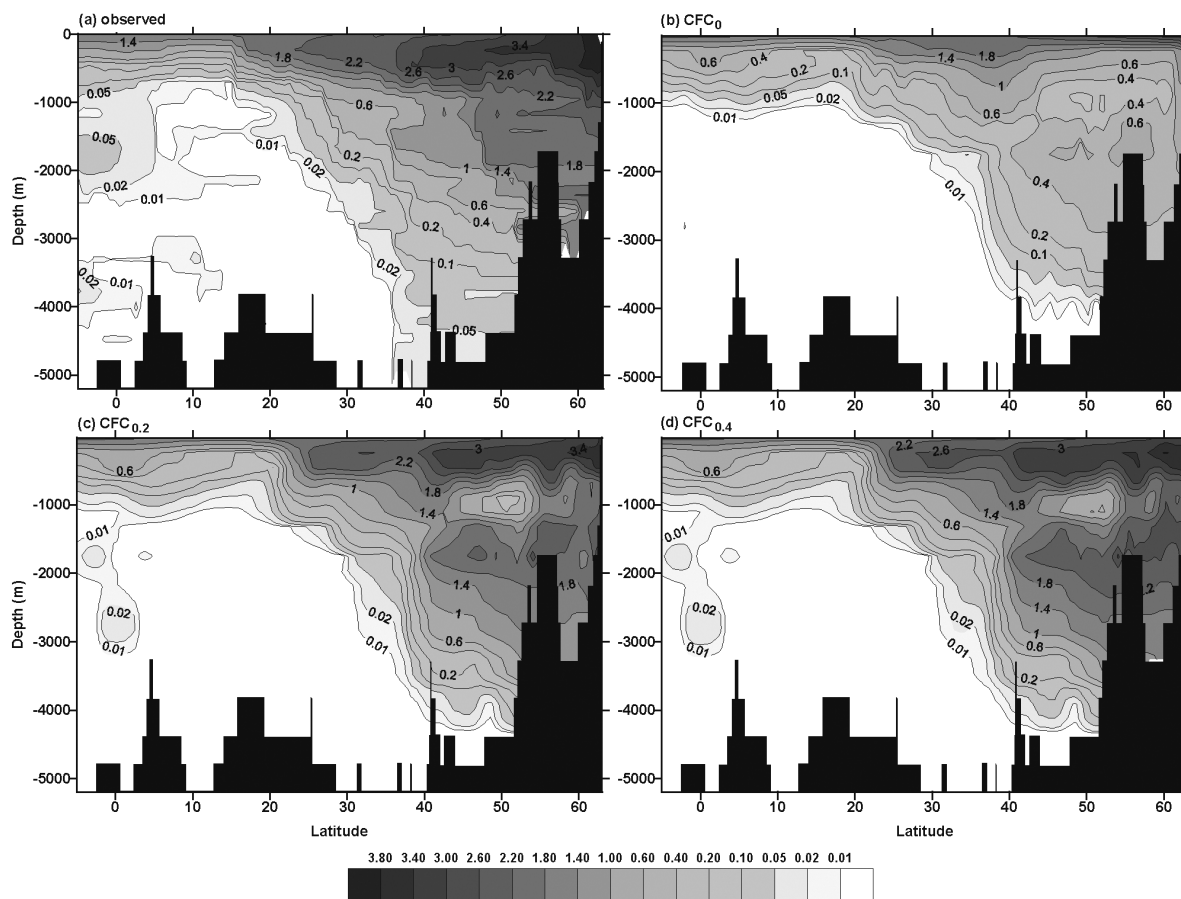


FIG. 2. CFC-11 concentration ( $\text{pmol kg}^{-1}$ ) for meridional NA20W section along  $20^{\circ}\text{W}$  in the North Atlantic (Aug 1993): (a) observed, (b)  $\text{CFC}_0$ , (c)  $\text{CFC}_{0.2}$ , and (d)  $\text{CFC}_{0.4}$ .

are persistent features of the equatorial region extending to at least  $10^{\circ}\text{W}$  for the upper jets that are not blocked by the Mid-Atlantic Ridge (Gouriou et al. 2001; Andrié et al. 1998). Eastward EEJs have been observed to occur symmetrically north and south of westward flowing equatorial deep jets (EDJs) that form a series of stacked eastward and westward flowing jets centered on the equator.

Many of the features observed along the NA20W section are captured by the  $\text{CFC}_{0.2}$  experiment (Fig. 2b). Mode water in the subtropical gyre has very similar meridional and vertical extent, although the bounding main thermocline is stronger due to a spurious CFC minimum below. This spurious feature is present in a number of the OCMIP models (Dutay et al. 2002, their Fig. 5) and also in the eddy-permitting North Atlantic simulation of Beismann and Redler (2003) who suggest that it is due to poor ventilation of subtropical mode water. This is unlikely, though, as the minimum is below the depth of observed mode water penetration. Moreover, in our model there is a distinct intrusion of low CFC water into this region as part of the North Atlantic Current, which at intermediate depths ( $\sim 1000$  m) corresponds to this minimum.

The front at the southern end of the subtropical gyre is more pronounced than observed and shifted almost  $5^{\circ}$  farther north. Deeper in the water column there is a strong LSW signal penetrating to  $\sim 40^{\circ}\text{N}$  centered at  $\sim 1700$  m; however, the deeper overflow water observed in the Iceland Basin ( $55^{\circ}$ – $60^{\circ}\text{N}$ ) is entirely absent because the model domain does not include the northern formation region where CFCs destined for the deeper NADW core would be absorbed. This is a clear weakness of the POCM in the context of global water-mass ventilation processes.

In the deep equatorial region the observed upper local tracer maximum is present between  $1^{\circ}$  and  $2^{\circ}\text{S}$  centered between 1750 and 2200 m, although it is significantly weaker than observed. A further maximum is present at the same position north of the equator (although at concentrations below the lowest contour value) indicating the existence of an EEJ pair at this depth, with the southern jet supplied with greater levels of tracer. Between 2750 and 3300 m centered directly on the equator is a strong maximum. This represents the spurious advection of tracer advected in an EDJ from the DWBC at a depth that, in reality, would sit between the double DWBC core and so would be depleted in CFCs. The

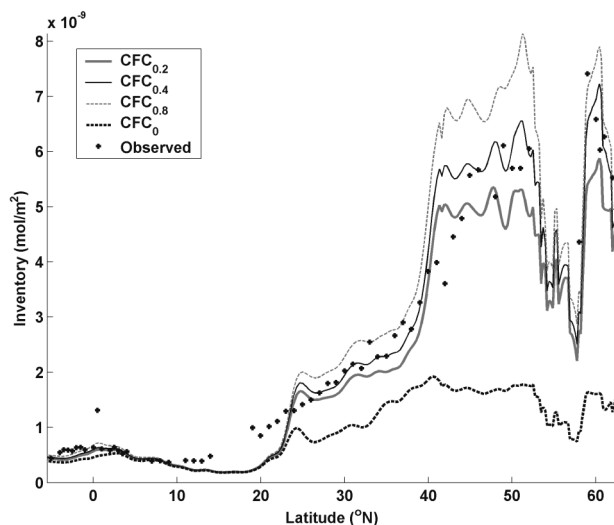


FIG. 3. CFC-11 column inventory ( $\text{mol m}^{-2}$ ) along NA20W section for observations and experiments  $\text{CFC}_0$ ,  $\text{CFC}_{0.2}$ ,  $\text{CFC}_{0.4}$ , and  $\text{CFC}_{0.8}$ .

source region for lower NADW occurs north of the model domain and as a result CFC does not have a surface connection to this water mass. As one would therefore expect, no CFC-laden core is evident at the position of the observed EEJ fed by the deeper variety of NADW.

Distributions for  $\text{CFC}_{0.4}$  (Fig. 2d) and  $\text{CFC}_{0.8}$  (not shown) along NA20W are qualitatively very similar to the  $\text{CFC}_{0.2}$  experiment. This is the case for all other sections that we analyzed. The deeper mixed layers in  $\text{CFC}_{0.4}$  and  $\text{CFC}_{0.8}$  flux greater quantities of CFC into the ocean interior, but they do not alter the basic structure of ocean ventilation simulated in the offline model. In this manner, the ventilation pathways are relatively insensitive to the choice of MLD parameterization. In view of this, only CFC sections for  $\text{CFC}_{0.2}$  (where MLDs

most closely match those observed) are shown in the remainder of this chapter.

Without mixed layer overturning of CFCs, the  $\text{CFC}_0$  run lacks any of the LSW mode water formed in the surface mixed layers (Fig. 2b). Inventories show that north of  $\sim 22^\circ\text{N}$  the mixed layer plays a significant role in ventilation (Fig. 3). The inventories also reveal that away from the SACW/NACW front  $\text{CFC}_{0.2}$  performs well and is in quantitative agreement with the observations, although with underestimated values at  $45^\circ$ – $55^\circ\text{N}$  as a result of the spurious subsurface minimum, discussed above.

The continued southward passage of NADW is captured by the WOCE A5R section along  $24^\circ\text{N}$  [referred to as A24N in Dutay et al. (2002)], at the start of 1998 (Fig. 4) (Peltola et al. 2001). The observed section shows the distinct upper and lower cores of the DWBC. Once again the offline model does not have any lower core maximum, although an elevated signal does penetrate below 4000 m. In addition the upper core is constrained too close to the continental margin, with little signal extending east of  $70^\circ\text{W}$ . The meridional WOCE A20 section (Fig. 5) from 1997 [not part of the Dutay et al. (2002) analysis] intersects the DWBC on either side of the A5R section. Double cores are observed at both extents of the section centered at  $\sim 1000$  and  $\sim 4500$  m to the north and at  $\sim 1800$  and  $\sim 4000$  m to the south. In the north, the solitary modeled upper core is too deep at  $\sim 1800$  m, while to the south the upper core occurs near the observed core depth. The zonal extent of the upper core is significantly better than for A5R although still less than observed.

Figure 6 shows the observed outflow of upper NADW from Smethie et al. (2000) (normalized to a common date of 1990) and the equivalent modeled  $\text{CFC}_{0.2}$  section on  $\sigma_{1.5} = 34.51$ . Both plots show strong meridional gradients in the western basin between  $30^\circ$  and  $40^\circ\text{N}$ . South of this the only penetration is via the DWBC that

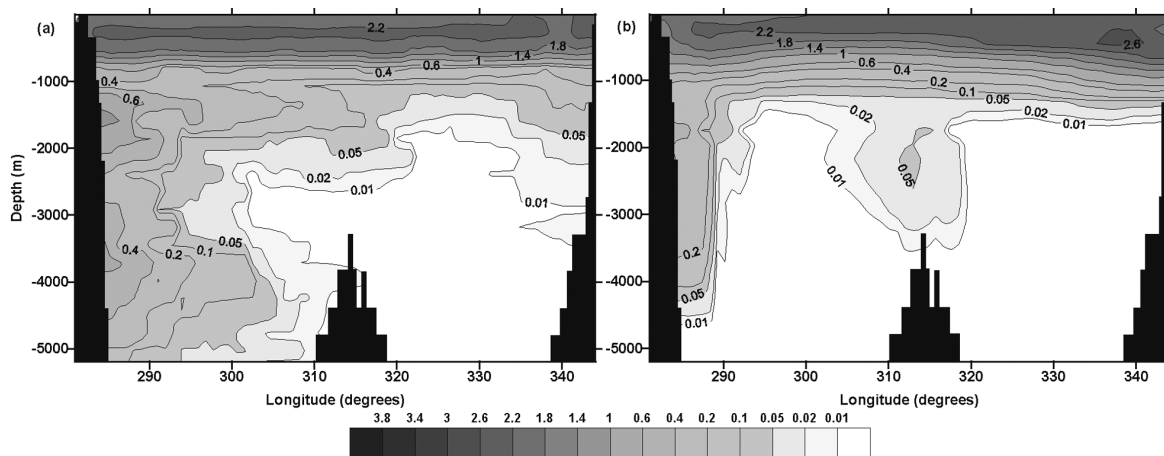


FIG. 4. CFC-11 concentration ( $\text{pmol kg}^{-1}$ ) along zonal WOCE AR5 section along  $\sim 24^\circ\text{N}$ : (a) observed (Jan–Feb 1998) and (b)  $\text{CFC}_{0.2}$  (Jan 1998).

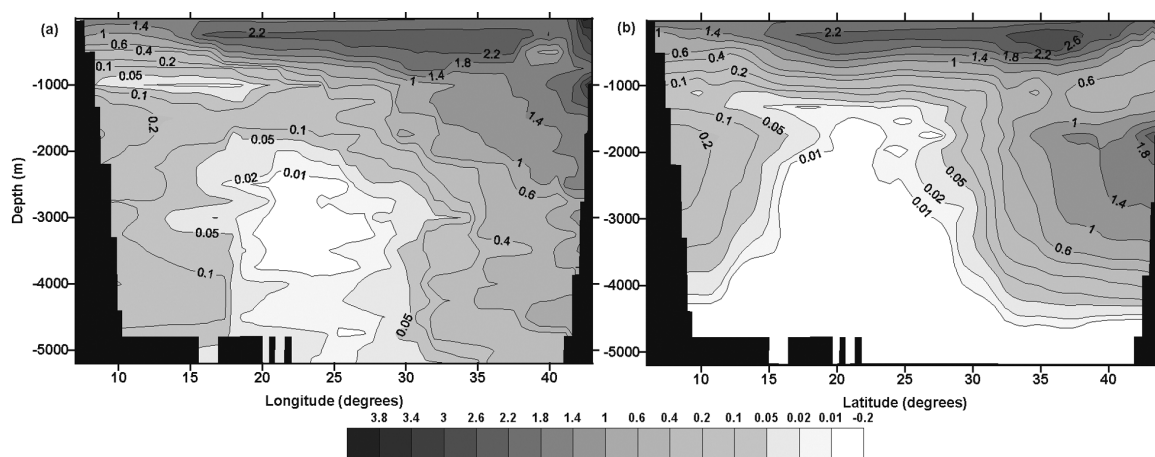


FIG. 5. CFC-11 concentration ( $\text{pmol kg}^{-1}$ ) along meridional WOCE A20 section ( $\sim 52^\circ\text{W}$ ): (a) observed (Jan–Feb 1998) and (b)  $\text{CFC}_{0.2}$  (Jan 1998).

branches at the equator, one part continuing as a DWBC into the Southern Hemisphere and the other heading across the Atlantic, constrained close to the equator. As evidenced in the individual sections, the  $\text{CFC}_{0.2}$  DWBC signal does not spread far enough to the east, with a tight outflow locked to the western boundary. This is likely due to the lack of sufficient lateral eddy mixing in this region where eddy activity would be expected to be high—a consequence of the temporal averaging of the advection fields or because the model fails to capture small-scale recirculations that transport CFCs eastward in observation.

#### b. Pacific Ocean

Figure 7a shows CFC-11 observations from the WOCE P13 cruise nominally along  $165^\circ\text{E}$  in the North

Pacific during 1992. No significant CFC signal is observed below  $\sim 2000$  m. Features observed along this section are very similar to previous meridional sections in the western basin during 1987 and 1988 (Warner et al. 1996). Deepest penetration depths ( $> 1100$  m) occur within the subtropical gyre at  $\sim 30^\circ\text{--}35^\circ\text{N}$ . Penetration depths and inventories (Fig. 8) decrease southward with a front evident at the North Equatorial Current and Countercurrent divergence, at  $\sim 10^\circ\text{N}$ . The subtropical gyre comprises primarily Subtropical Mode Water (STMW) formed by shallow winter convection, near the northeastern limit of the gyre and advected laterally into the gyre (Suga and Hanawa 1997), and within the lower thermocline by North Pacific Intermediate Water (NPIW) formed through deep mixing in the Sea of Okhotsk (Warner et al. 1996). Penetration depths in the

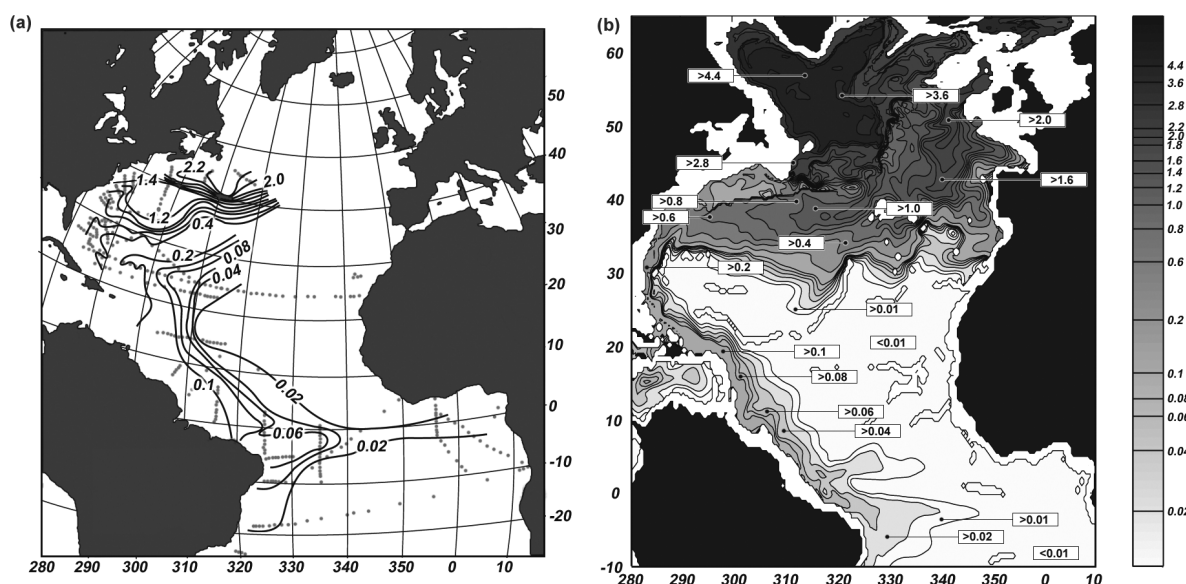


FIG. 6. Lateral CFC-11 concentrations ( $\text{pmol kg}^{-1}$ ) for ULSW: (a) observed distribution from Smethie et al. (2000) (data normalized to a common date of 1990) and (b)  $\text{CFC}_{0.2}$  distribution on  $\sigma_{1.5} = 34.51 \text{ kg m}^{-3}$  during Jun 1990.



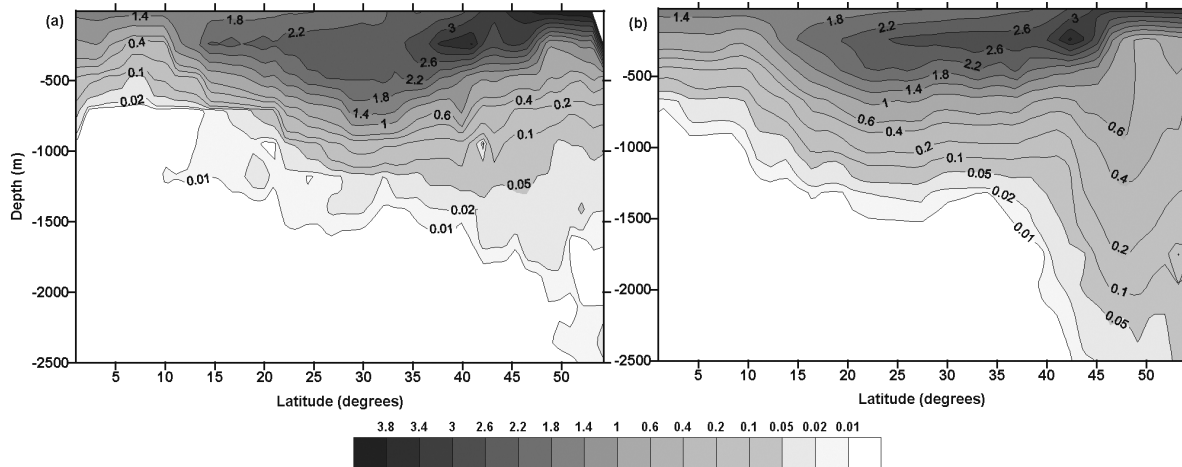


FIG. 7. CFC-11 concentration ( $\text{pmol kg}^{-1}$ ) along meridional WOCE P13 section ( $\sim 165^\circ\text{E}$ ): (a) observed (Aug–Oct 1992) and (b)  $\text{CFC}_{0.2}$  (Aug 1992).

subpolar gyre are much shallower ( $\sim 400$  m), a result of the strong stratification and upwelling of low CFC concentration deep waters.

$\text{CFC}_{0.2}$  shows good qualitative agreement with observations: shallow penetration in the subpolar region, increasing in the subtropical gyre with the intrusion of subsurface, high concentration mode water, and a weak front once again across the north equatorial divergence. North of  $\sim 25^\circ\text{N}$  tracer inventories are generally underestimated. With no mixed layer deepening during winter the  $\text{CFC}_0$  run shows no mode water formation, only the recently ventilated waters being advected from the Sea of Okhotsk ( $\sim 45^\circ\text{N}$ ). The lack of STMW formation is a common feature to all the OCMIP models

(Dutay et al. 2002). The maximum penetration depth in our model  $\text{CFC}_{0.2}$  run is more than 200 m shallower than observation and occurs too far south.

### c. Southern Ocean

Offline simulations are compared with two meridional CFC sections: (i) the AJAX section (Fig. 9a) along the Greenwich meridian in 1983 (Warner and Weiss 1992) and (ii) the WOCE P15 section (Fig. 10a) along  $190^\circ\text{E}$  in 1996. The observations reveal that the most extensive area of newly ventilated water is the mode water, which has an almost circumpolar extent and is formed by open ocean convection. This water travels northward in the

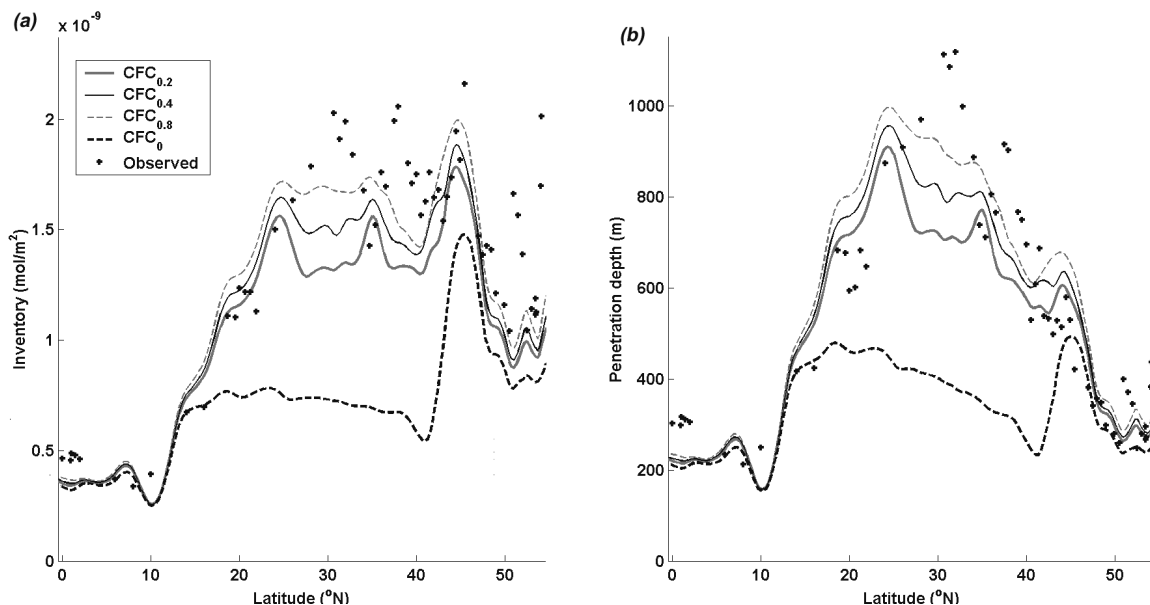


FIG. 8. (a) CFC-11 column inventory ( $\text{mol m}^{-2}$ ) and (b) penetration depths (m), along the WOCE P13 section for observations and experiments  $\text{CFC}_0$ ,  $\text{CFC}_{0.2}$ ,  $\text{CFC}_{0.4}$ , and  $\text{CFC}_{0.8}$ .

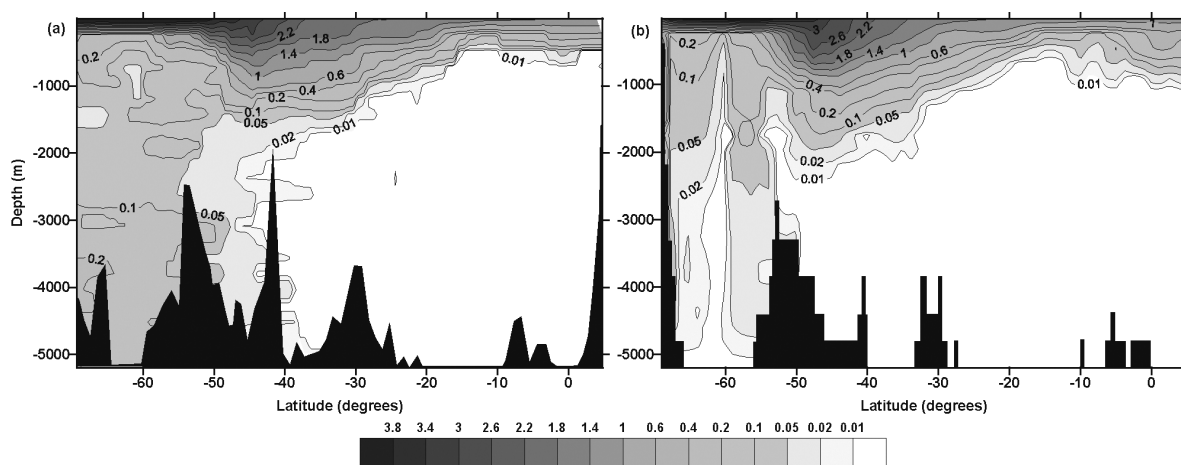


FIG. 9. CFC-11 concentration ( $\text{pmol kg}^{-1}$ ) for AJAX section along Greenwich meridian: (a) observed (1983–84) and (b)  $\text{CFC}_{0.2}$  (Dec 1983).

subtropical gyres as Antarctic Intermediate Water (AAIW). Other formation mechanisms for AAIW have been postulated including subduction along steep isopycnals and subsurface mixing; however, the relative importance of these processes is still in question (e.g., Saenko et al. 2003; Santoso and England 2004). South of the ACC poorly ventilated Circumpolar Deep Water (CDW), which may have undergone many circuits around Antarctica, rises near the Antarctic “Divergence.”

Both sections show these generic Southern Ocean watermass features. Mode waters in the subtropical gyres have their greatest penetration depths (not shown) between  $45^{\circ}$  and  $55^{\circ}\text{S}$  (P15) and between  $40^{\circ}$  and  $50^{\circ}\text{S}$  (AJAX) reaching depths  $>1200$  m and  $>750$  m, respectively. Inventories gradually decrease northward (Fig. 11), although the AJAX section shows a small increase in the equatorial region where the surface waters are subducted into the interior in a tropical over-

turning cell. Below the ventilated intermediate water and extending southward CFC concentrations are low because of the intrusion of CDW. Close to the Antarctic margin at greater depths newly ventilated AABW brings elevated concentrations of CFC, although concentrations are substantially lower than surface values, as a result of significant entrainment of poorly ventilated water during downslope flow. Once again, there is generally a good qualitative agreement between simulations and observations at surface and intermediate depths (Figs. 9 and 10). Column inventories are of a similar structure (Fig. 11), although the observed northwards spread of intermediate water is greater than in the model.

Upwelling of CFC-depleted CDW is well placed (near  $60^{\circ}\text{S}$ ); however, both sections exhibit model column inventories substantially lower than observed (especially for P15). The diminished eddy mixing of the offline model in this area—normally associated with high eddy activity—would reduce the lateral transport of tracer

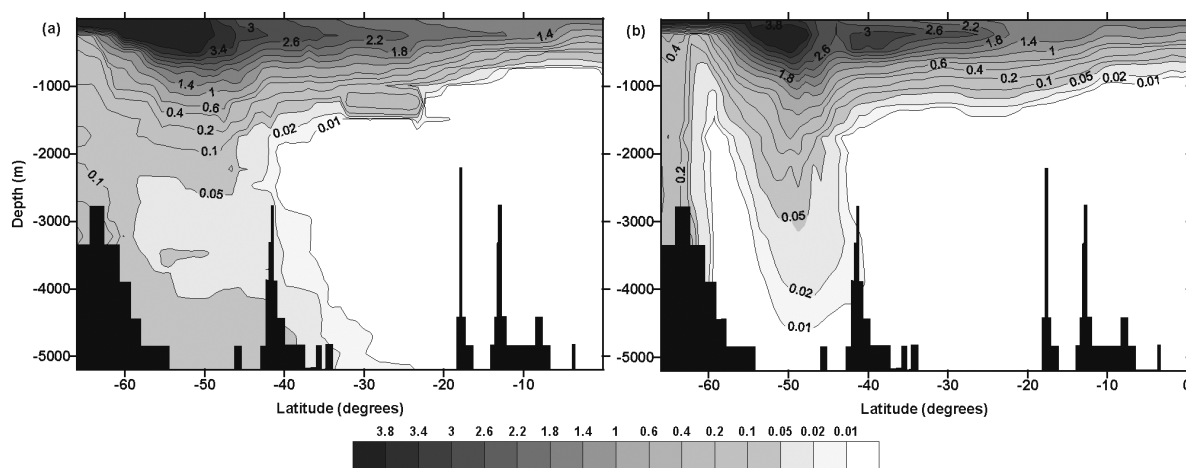


FIG. 10. CFC-11 concentration ( $\text{pmol kg}^{-1}$ ) along WOCE P15 section ( $\sim 170^{\circ}\text{W}$ ): (a) observed (Jan–Feb 1996) and (b)  $\text{CFC}_{0.2}$  (Feb 1996).

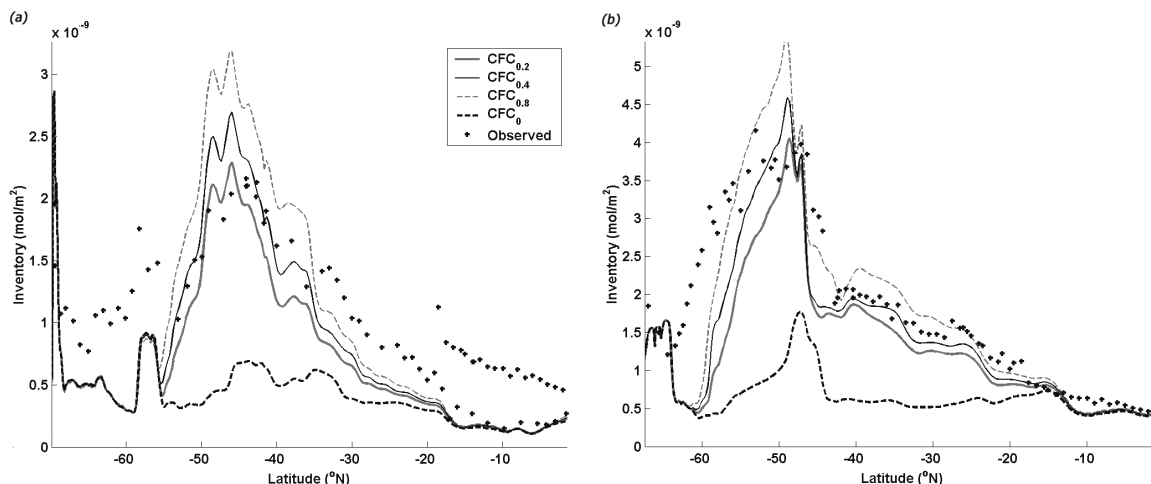


FIG. 11. CFC-11 column inventory ( $\text{mol m}^{-2}$ ) for observations and experiments  $\text{CFC}_0$ ,  $\text{CFC}_{0.2}$ ,  $\text{CFC}_{0.4}$ , and  $\text{CFC}_{0.8}$  along (a) AJAX section and (b) WOCE P15 section.

into these depleted regions, thus emphasizing the pronounced signal of low tracer concentration. This low CFC inventory is unlike many coarse resolution ocean models that typically mix excessive amounts of CFC downwards at these latitudes. This is evident in the column inventories of the OCMIP models (Dutay et al. 2002, their Fig. 11). England and Hirst (1997) also see this in their coarse-resolution model experiments in which they use a variety of subsurface mixing parameterizations. They find that the overestimated CFC concentrations are directly related to deep convection that, in some experiments, penetrates almost to the ocean floor. The offline model MLD parameterization, on the other hand, shows no deep convection south of  $60^\circ\text{S}$  (Fig. 1). England and Hirst (1997) note improved results below 1000 m with the implementation of the Gent and McWilliams mixing parameterization, which results in more stratified conditions. Just north of the strongest upwelling, both simulated and observed AJAX sections show the intrusion of recently ventilated water that has been advected eastward along the northern limb of the Weddell gyre. Adjacent to the Antarctic margin, the offline model reproduces some elevated concentrations; however, in both cases, inventories are smaller than those observed. No significant bottom water signal can be seen extending northward at the abyssal depths along both AJAX and WOCE P15 sections. Formation of bottom water in OGCMs is often too weak in the Southern Ocean as a result of the poorly sampled and summer-biased observational data that are used to force the model (e.g., Doney and Hecht 2002). In addition downslope flow is particularly sensitive to the representation of bottom topography, and the steplike nature of  $z$ -level models has been shown to inhibit these flows (Beckmann and Döscher 1997).

A recent analysis of WOCE sections in the Southern Ocean by Orsi et al. (1999) shows the distribution of CFC within the AABW on the  $\gamma^n = 28.27 \text{ kg m}^{-3}$

neutral density surface (Fig. 12). According to Orsi et al. (1999), this represents the lower bound neutral density surface for Circumpolar Deep Water and, as such, surfaces exceeding this only contain water sourced on the Antarctic shelf. These dense waters are completely blocked at the Drake Passage and are thus decoupled from the overlaying eastward flowing Antarctic Circumpolar Current. Our simulated density values, calculated from the POCM temperature and salinity fields, tend to be slightly lower than observed. This is typical of  $z$ -level OGCMs (e.g., England and Hirst 1997). Consequently, for comparison with the observations we choose a neutral layer ( $\gamma^n = 28.22 \text{ kg m}^{-3}$ ) that more closely matches the lower limit for CDW surface. Waters along this surface in the offline model are still at sufficient depth to be blocked at the Drake Passage, and no contamination by intermediate water is evident.

The best model agreement is in the Weddell Sea, where waters forming in the western region flow clockwise along the northern perimeter of the Weddell gyre and then either northward near  $30^\circ\text{W}$  as a western boundary current into the Argentine Basin or back towards the south and west near  $10^\circ$ – $20^\circ\text{E}$ . A deep minimum is evident in the central Weddell gyre region. A region of high tracer concentration ( $>1.6 \text{ pmol kg}^{-1}$ ) stretches from the western Weddell Sea to  $\sim 20^\circ\text{E}$ , adjacent to the margin. A similar pattern is seen in the Ross Sea; waters forming in the western part of the sea flow clockwise and then either recirculate at the eastern edge of the Ross gyre or continue eastward while moving closer to the continental margin. Concentrations are, however, generally lower than the observed by a factor of 2 or more. A strong signal is also evident near the Adelie coast ( $140^\circ$ – $150^\circ\text{E}$ ), but this fails to extend westward as observed, and the region of coastal waters between  $150^\circ$  and  $50^\circ\text{E}$  are devoid of the high observed concentrations that flow eastward from the Adelie coast and the Amery Ice Shelf (Orsi et al. 1999, their Fig.

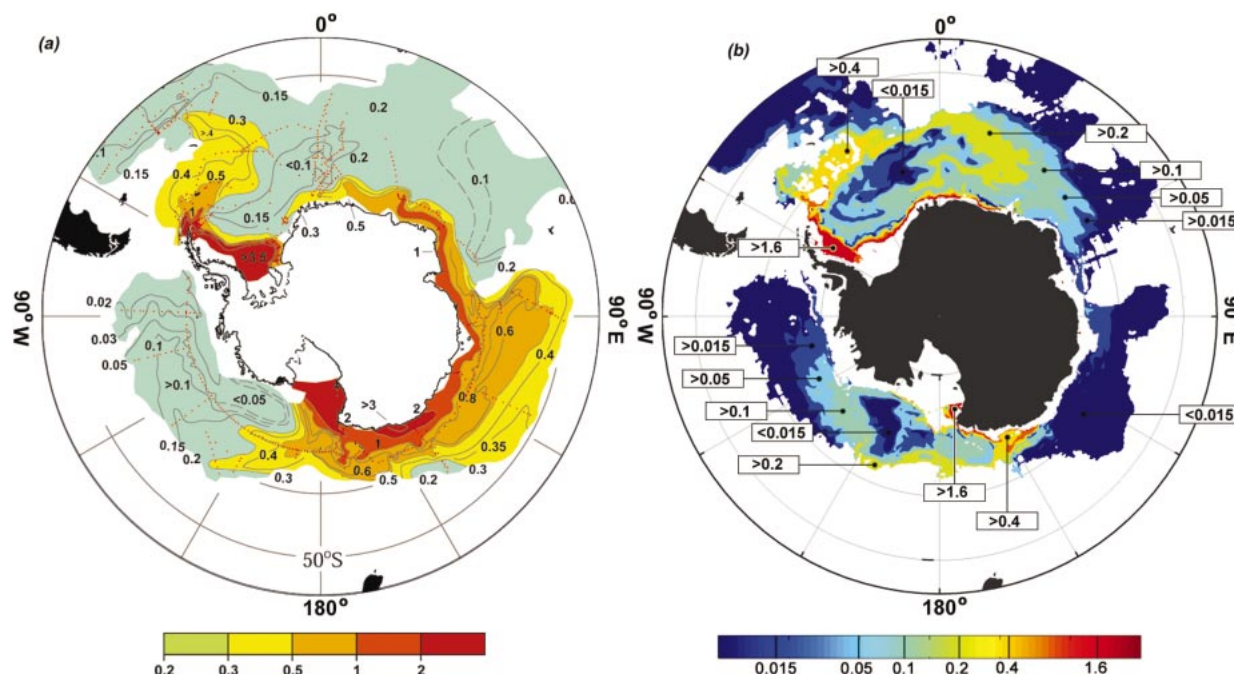


FIG. 12. CFC-11 distribution of bottom water on neutral density surface: (a)  $\gamma^n = 28.27 \text{ kg m}^{-3}$  (normalized to 1990) from Orsi et al. (1999) and (b)  $\gamma^n = 28.22 \text{ kg m}^{-3}$  for CFC<sub>0.2</sub> experiment (Jun 1990).

7e). In these instances, the offline model is lacking realistic interior ocean convective overturning and downslope flows. Generally both model and observed neutral density surfaces are significantly deeper in this area than in the Weddell Sea region where agreement with observed CFC is better. Quantitative agreement also tends to get worse extending eastward out of the Ross Sea where density surfaces also deepen.

#### 4. Results from passive tracer experiments

Although there are substantial areas of agreement between observed and simulated CFC distribution, it is apparent that some of the ventilation pathways into the deep ocean are too weak or entirely missing (e.g., overflow water in the North Atlantic and certain varieties of AABW). The use of prescribed tracer source regions beneath the ocean surface allow interior ventilation pathways to be examined in more detail. It also provides an opportunity to investigate longer time-scale ventilation processes, beyond the scope of recently introduced anthropogenic CFCs. For example, we analyze where NADW and AABW resurface in the model over a 1000-yr integration, as well as assessing the multi-century advection pathways in the ocean interior. The following results are from two 1000-yr experiments using the same model parameterizations as the CFC<sub>0.2</sub> experiment, with tracer sourced in the deep North Atlantic and Antarctic Oceans (for details of the passive tracer see section 2c).

For multicentennial time scales, useful comparisons can

be made with quantities derived from  $^{14}\text{C}$  data. Natural  $^{14}\text{C}$ , with a lifetime of 5730 years, and the corresponding derived quantity  $\Delta^{14}\text{C}$ , the deviation of the  $^{14}\text{C}/^{12}\text{C}$  ratio from the preindustrial isotopic ratio, provides an indication of the time expired since a water mass was last in contact with the surface (England and Maier-Reimer 2001). Lowest  $\Delta^{14}\text{C}$  values indicate waters that have been remote from the surface for the most amount of time. In order to make a semiquantitative comparison with model data,  $\Delta^{14}\text{C}$  and passive tracer concentrations can be converted to “age” values. For a given  $\Delta^{14}\text{C}$  value a corresponding “advection-age” may be derived, which represents the time since the water was last at the surface, assuming purely advective transport (i.e., no mixing),

$$\text{age}_{\text{advection}} = -\tau \ln\left(\frac{X}{1000} + 1\right), \quad (4)$$

where  $\tau$  is the decay constant for  $^{14}\text{C}$  (8267 years) and  $X$  is the  $\Delta^{14}\text{C}$  value (ppt). In the case of analyzing the abyssal ventilation time scales out from the Antarctic region, the advection ages are calculated referenced to a year-0 value for  $\Delta^{14}\text{C} = -150$  ppt, which represents the typical  $\Delta^{14}\text{C}$  at depth close to the Antarctic margin.

The modeled passive tracer time series,  $C(t)$ , can be used to calculate an “age spectrum,”  $\psi(t)$  (Hall et al. 2002). This fundamental property represents a probability distribution of ages that go into making up a given water parcel. A weighted average of  $\psi(t)$  then gives the mean tracer age, such that



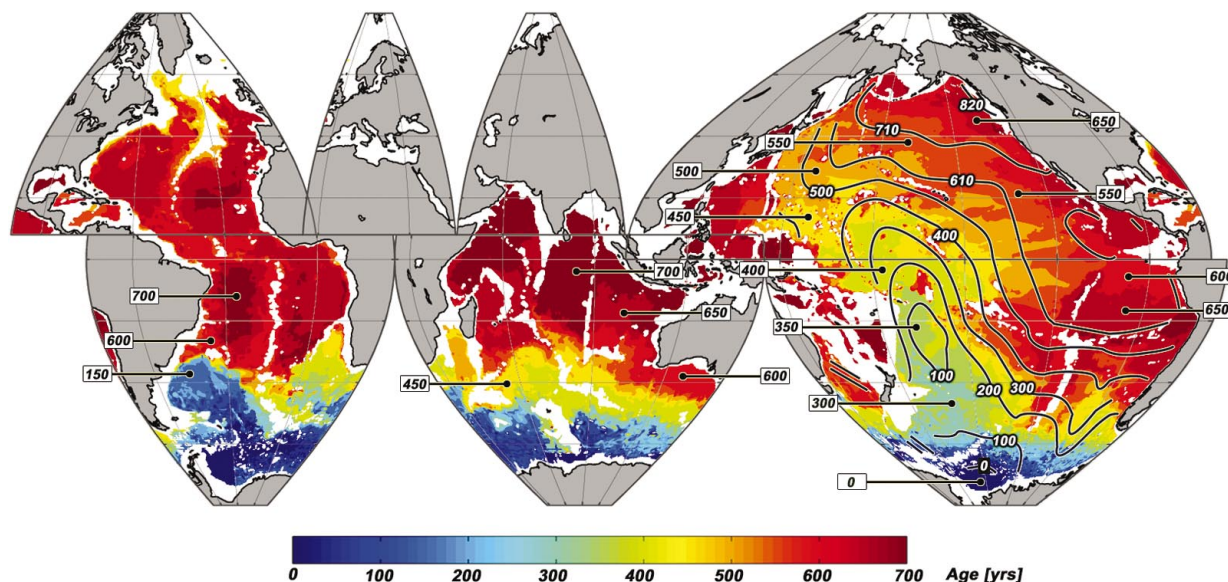


FIG. 13. Tracer age at the deepest model level, where depth is at least 3300 m (filled contours and black text) with  $\Delta^{14}\text{C}$  derived advection age (yr) superimposed in the Pacific Ocean (black lines with white text).

$$\text{age}_{\text{tracer}} = \frac{\int_0^{\infty} t \psi \, dt}{\int_0^{\infty} \psi \, dt}, \quad (5)$$

where  $\psi(t) = dC/dt$ . Resource limitations mean that the current experiments have not been run out to steady state for the passive tracer. As such the tracer age represents an underestimation of the steady-state value, or “ideal age,” and convergence between these two ages becomes worse for older age values, which are further from equilibrium. In comparing the above ages, it should also be noted that the radiocarbon age estimate will also be younger than the true age because mixing is nonnegligible.

#### a. Bottom water pathways

In the deep ocean the most significant northward penetration of southern-origin water is in the western Pacific, ventilated by the northward flow of bottom water as a western boundary current along the Kermadec–Tonga Trench system (Whitworth et al. 1999). Further flow into the central Pacific is primarily through the Samoan Passage where the pathways become more complicated (Kawabe et al. 2003). Schlosser et al. (2001) present a map of bottom  $\Delta^{14}\text{C}$  derived from the WOCE and GEOSECS datasets. Relatively high  $\Delta^{14}\text{C}$  values, associated with recently ventilated CDW, are observed east of the Kermadec–Tonga Trench system and extend into the Northern Hemisphere where the predominant implied pathway turns westward and continues clockwise around the Northwest Pacific Basin to at least the

Aleutian Island “Arch” (Schlosser et al. 2001). Diffuse fingers of higher  $\Delta^{14}\text{C}$  are also evident penetrating the northern and northeastern basin. Lack of sampling resolution makes it impossible to pinpoint more specific pathways from the  $\Delta^{14}\text{C}$  distribution. The least ventilated waters, with lowest  $\Delta^{14}\text{C}$  values, are across the northeast of the basin. Low values extend from here along the eastern rim of the Pacific basin as far south as the Peru Basin ( $\sim 20^\circ\text{S}$ ).

Figure 13 shows bottom tracer age (where water depth is at least 3300 m). Superimposed are contours of derived advection age (reconstructed from Schlosser et al. 2001, their plate 5.8.17). There is good qualitative agreement between passive tracer and  $\Delta^{14}\text{C}$  ages: youngest ages appear along the Kermadec–Tonga Trench system with low age protruding north to  $\sim 20^\circ\text{N}$ , where a major part of the flow moves eastward out of the Samoan Passage. Old waters extend from the northeast Pacific, along the American continental margin, and south into the Peru Basin. The oldest simulated tracer values are adjacent to the continental margin, in agreement with other numerical ocean models that incorporate  $^{14}\text{C}$ , but in contrast to the observed  $\Delta^{14}\text{C}$  age, which has the oldest waters removed from the coast (Schlosser et al. 2001). Even though there is a reasonable qualitative match, advection ages and tracer ages differ considerably, especially at each end of the age range. For newly ventilated waters, model ages are significantly greater than advection ages as the model tracer is influenced by mixing with older, tracer-free waters. Conversely for older water, advection ages are older than model ages, a consequence of the passive tracer field not having come to a final equilibrated state. If integrations were extended out to full equilibrium, these ages would be

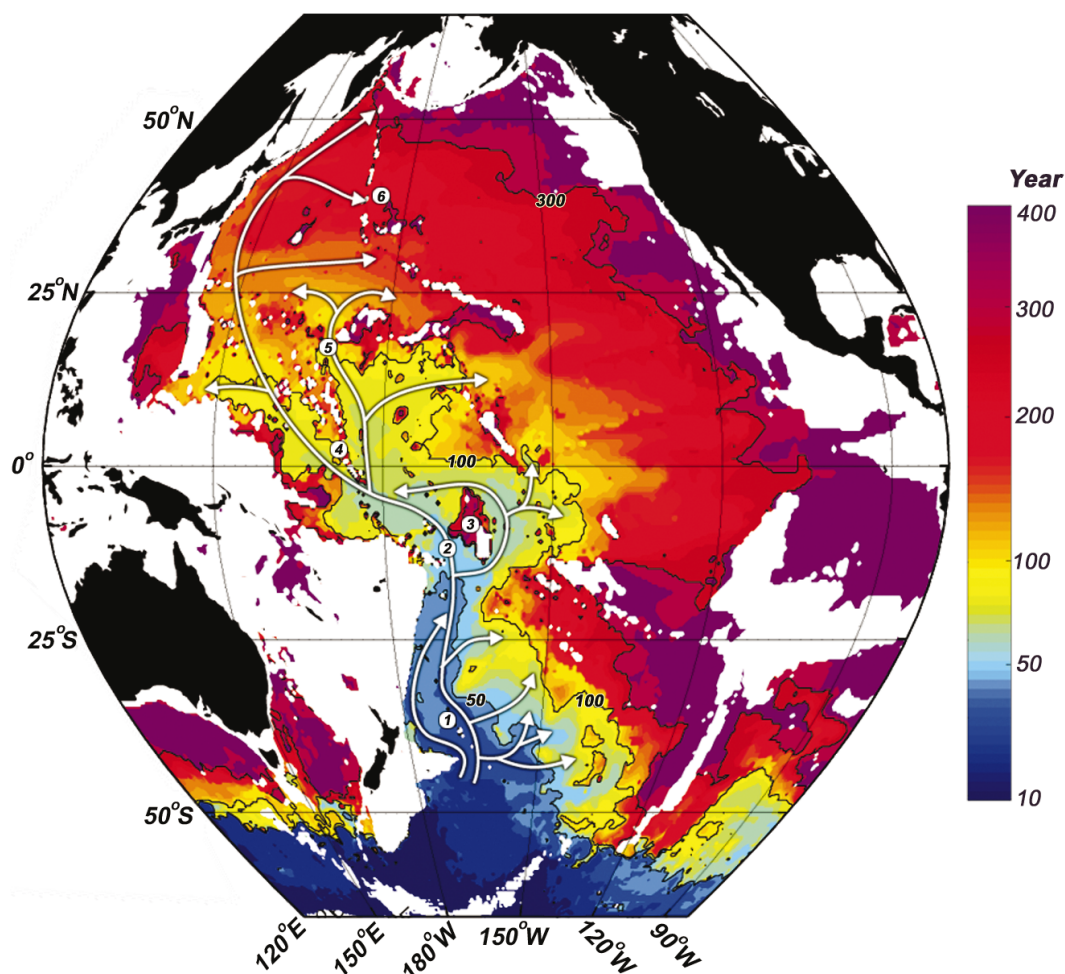


FIG. 14. Time evolution of the 1% passive tracer concentration front, shown every 10 yr for the first 200 yr then at 250, 300, and 400 yr (black contour lines show 50-, 100-, and 300-yr contours). Superimposed are the major implied pathways. Legend: 1—Louisville Ridge; 2—Samoan Passage; 3—Manihiki Plateau; 4—Gilbert Ridge; 5—Wake Island Passage; 6—Main Gap.

expected to increase somewhat. A global coarse-resolution tracer age simulation by England (1995), which was run out to equilibrium (taking 5000 years of integration) showed maximum ages in the North Pacific at middepths of almost 1500 yr. This coarse model is in broad qualitative agreement with our offline model and with observations (England 1995, his Fig. 4d). However, the young-age signal extending along the Kermadec–Tonga Trench system extends only as far as the equator, a possible consequence of the sluggish boundary currents evident in low-resolution models.

By looking at the time evolution of the model tracer field it is possible to identify the major bottom-water ventilation pathways into the North Pacific. Figure 14 shows the evolution of the 1% tracer concentration contour (at 10-yr intervals for the first 200 years and thereafter at 220, 250, and 300 years) with the major implied pathways superimposed. The simulated flow into the Pacific basin occurs via two deep western boundary

currents along the Kermadec–Tonga and Louisville Ridge systems that merge as the trenches come together, both flows are greatest at the deepest model levels. The zonal WOCE P6 section across 32°S of  $\Delta^{14}\text{C}$  (Schlosser et al. 2001) shows two areas of maximum  $\Delta^{14}\text{C}$ , the first flanking the Kermadec–Tonga Ridge between 3500 and 4500 m (well above the seafloor) and the second east of the Louisville Ridge at the bottom. The majority of northward flow travels through the Samoan Passage, with a smaller flow that passes anticlockwise around the Manihiki Plateau, to the east of the passage, in broad agreement with observations (Roemmich et al. 1996). Some of this eastern flow fills the Penrhyn Basin to the east, with the remainder continuing westward along the northern side of the plateau. The flow that has transited through the Samoan Passage moves westward to the Gilbert Ridge where it again bifurcates. The eastern flow branches again at the northern edge of the Central Pacific Basin, with one part heading east toward the north-

east Pacific basin and the other entering the Northwest Pacific Basin through Wake Island Passage. The western branch continues northward, constrained to the west by the ridge systems west of the Marian/Izu–Ogasawara trenches and farther north by the continental margin. This is consistent with hydrographic measurements taken by Kawabe et al. (2003) and the general description given by Mantyla and Reid (1983). Farther north, a synthesis of various studies of the Northwest Pacific Basin is presented by Owens and Warren (2001). This provides evidence of further pathways, in particular two eastward branches off the western boundary current: one north of 25°N that travels into the northeastern basin north of the Hawaiian Ridge; the other through the “Main Gap” in the Emperor Sea Chain. The north-eastward flow of the western boundary current is also seen to continue towards the Aleutian Trench. These are also the primary pathways followed by the simulated tracer. Although some of the detailed flow pathways are different between simulation and observation, overall agreement is good and much of the discrepancy is a result of finescale differences in the bathymetry that play a major role in determining abyssal flow pathways.

Simulated northward flow into the Atlantic and Indian basins is far less pronounced than in the Pacific with little tracer reaching into the Northern Hemisphere. In the Indian Ocean, northward penetration of simulated bottom water occurs through a number of deep gaps in the bounding ridge systems. A gap in the Southwest Indian Ridge south of South Africa feeds the Agulhas and Mozambique Basins, with water derived from the Weddell Sea, where tracer is subsequently blocked from continuing any farther northward by shallow topography in the Mozambique Channel and by the Madagascar Ridge to the east. AABW from the Weddell and Amery regions also flows around the western side of the Kerguelen Plateau and fills the Crozet Basin, with flow around the east of the plateau hindered by shallower topography. A weak signal can be seen emanating from the Crozet Basin through channels in the Southwest Indian Ridge and into the Madagascar Basin from where it continues northward as a western boundary current along Madagascar. These pathways correspond to observed Indian Ocean outflows of water leaving the Weddell Sea (Haine et al. 1998; Mantyla and Reid 1995). A further pathway is evident sourced from the east where AABW fills the Australian–Antarctic Basin and continues northward through the Southeast Indian Ridge via the Australian–Antarctic “Discordance.” This route between the basins is clearly seen in the property maps of Mantyla and Reid (1995). Flow continues westward and northward along the northern flank of the ridge into the central Indian Ocean. Pathways into the Northern Hemisphere are more diffuse although some penetration is evident on both sides of the central Indian Ridge with little signal in the eastern basin.

In the Atlantic, much of the simulated tracer sourced from the Weddell Sea region is blocked from direct

northward transport by a system of ridges, primarily the South Scotia Ridge. Some northward movement is evident through gaps into the Scotia Sea; however, the majority of the tracer destined to go north first travels east around the South Sandwich Trench. Arhan et al. (1999) identifies three routes for Weddell Sea Water into the Argentine Basin (the northern limit of the majority of northward flowing water): (i) across the relatively shallow Falkland Plateau (~2500 m), (ii) through a wide breach in the Falkland Ridge (~35°–40°W), and (iii) to the east of the Islas Orcadas Ridge (~25°W). The model bathymetry however, dictates that the only significant simulated deep pathway is via the third, eastern, option. The simulated filling of the Argentine Basin is via a network of pathways spanning the basin. In contrast, Orsi et al. (1999) describe only a single pathway ventilating the Argentine Basin, sourced primarily through the the breach in the Falkland Ridge. In the eastern Atlantic, a weaker tracer signal, fed from water coming off the northeastern rim of the Weddell gyre that has exited the Southern Ocean through gaps in the Southwest Indian Ridge, penetrates as far north as the Namibia Abyssal Plain. The lack of vertical resolution at depth will necessarily imply that many small-scale pathways will not be in agreement with observation. In addition, the model’s representation of bathymetry is somewhat crude in certain locations (as also noted by Thorpe et al. 2004). Thorpe et al. note that bathymetry errors also result from the interpolation methods used to generate the POCM bathymetry. This model–observed mismatch in bathymetry drives some of the erroneous bottom water pathways noted above.

#### *b. Recirculation of bottom water*

At middepths  $> \sim 2000$  m, tracer concentrations across the basins are very low. In the Pacific region a comparison can be made along the zonal WOCE P6 section. Figure 15 shows a comparison between  $\Delta^{14}\text{C}$  advection ages at 32°S and the corresponding model-derived tracer age. Oldest ages are observed at middepths (~2000–3000 m) with two distinct maxima, at 155°W in the central Southwest Pacific Basin and at 75°W along the Chilean continental margin, both centered at ~2600 m. Schlosser et al. (2001) suggest that these correspond to two cores of the return flow of Pacific Deep Water, the ocean’s oldest water mass. Passive tracer results along the same section also show two areas of low tracer. The western area spreads from the Kermadec–Tonga Ridge into the Southwest Pacific Basin centered at a similar depth to the observed  $\Delta^{14}\text{C}$  age maximum. The eastern area again flanks the Chilean margin, but takes its oldest values at the deepest levels and extends too far to the west.

The fate of recirculated bottom water can be traced to the surface by assessing final concentrations of  $C_{\text{BW}}$  in the upper model level (Fig. 16) and the zonal mean of passive tracer (Fig. 17a) at year 1000. The majority



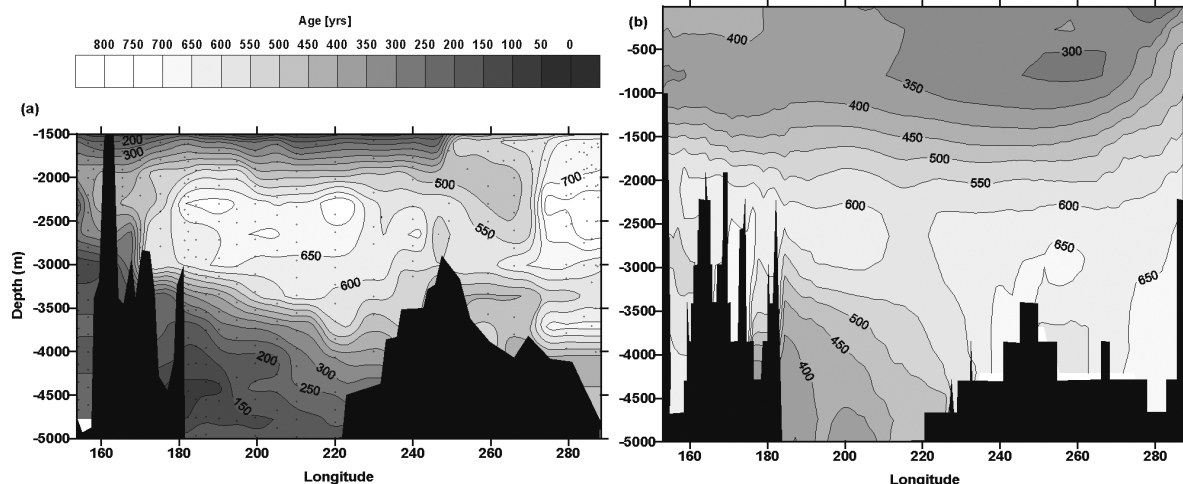


FIG. 15. Tracer age (yr) across the P06 section at 32°S. (a) Calculated from  $\Delta^{14}\text{C}$  values taking  $\Delta^{14}\text{C} = -150$  ppt to be zero age (bottom water close to the Antarctic margin has  $\Delta^{14}\text{C} \approx -150$  ppt). (b) Calculated using the 1000-yr "age spectrum" derived from  $C_{\text{BW}}$  concentrations integrated over 1000 yr.

of passive tracer upwells strongly close to the Antarctic margin and along the northern edges of the Weddell and Ross gyres, where the divergence of surface waters aids in pulling up deeper waters. Tracer levels remain high in these regions (south of the Antarctic divergence) and within the gyres where the tracer is quickly mixed. Some  $C_{\text{BW}}$  tracer gets mixed into the high energy ACC and is then zonally distributed throughout the Southern Ocean. Even though there is no explicit representation of tracer release at the formation regions of AAIW, entry into the Atlantic, Pacific, and Indian Oceans is predominantly as recycled intermediate water at depths between  $\sim 500$  and  $1500$  m (Fig. 17a). This is intensified in the eastern basin under the influence of the various anticyclonic subtropical gyres. In the Pacific there is an additional strong surface penetration of tracer in the eastern basin where mixed layers are deep (see Fig. 15, where young ages generally correspond to high tracer concentrations). Lowest ages are at intermediate depths and near the surface in the eastern Pacific. Farther north the elevated tracer values within intermediate water becomes less distinct, practically disappearing north of the zone of influence of the subtropical gyres, as basinwide upwelling moves the tracer into the surface layers.

### c. North Atlantic Deep Water

Figure 18 shows passive tracer from  $C_{\text{NADW}}$  at the depth of maximum outflow (centered at 2475-m depth) after 100, 300, and 1000 years of integration. This depth is below the upper NADW core tagged by CFC discussed in section 3a. From the source region two predominant deep pathways are evident. A clear signal travels along the eastern boundary of the Mid-Atlantic Ridge (MAR) centered at or above the top of the ridge. Large quantities of tracer leak westward across the top of the ridge and through the numerous fracture zones.

Below  $\sim 25^\circ\text{N}$  the signal dies away as the ridge becomes deeper. Hydrographic sections investigating the spread of LSW, taken over an 8-yr period in the region of the Azores Plateau (Paillet et al. 1998), show a persistent current above the eastern flank of the MAR that extends at least as far south as the Oceanographer Fracture Zone ( $\sim 34^\circ\text{N}$ ) where much of the flow feeds into the western basin.

The second pathway is the distinct DWBC along the American continental margin. Zonal tracer sections (not shown) reveal that the core of this flow generally remains centered at a depth of  $\sim 2500$  m, with elevated concentrations of tracer often evident between the position of the observed double cores that represent upper and lower NADW. Many of the climate models investigated by Dutay et al. (2002) show a similar single CFC maximum at this intermediate depth. Like the passive tracer, the POCM meridional velocities (not shown) show no double core. This implies that the missing core is not simply due to the lack of realistic tracer ventilation into the interior at the tracer source region, but is likely to be the result of poorly represented overflow processes (resulting in excessive entrainment of surrounding water) south of the Greenland–Iceland–Scotland ridges. In an eddy-permitting model of the Atlantic, Beismann and Redler (2003) only obtain a lower core once a BBL scheme is incorporated into their model. In the case of our CFC experiments a well-situated upper core is reproduced, demonstrating the ability of the model to form realistic waters to feed the upper core. In contrast the northern limit of the POCM simulation ( $\sim 65^\circ\text{N}$ ) precludes the lower CFC core originating in the Greenland–Iceland–Norwegian Sea. The DWBC can be traced down as far as  $\sim 45^\circ\text{S}$  where it abruptly turns eastward and is advected in a broad flow (initially between  $40^\circ$  and  $45^\circ\text{S}$ ) as part of the ACC.



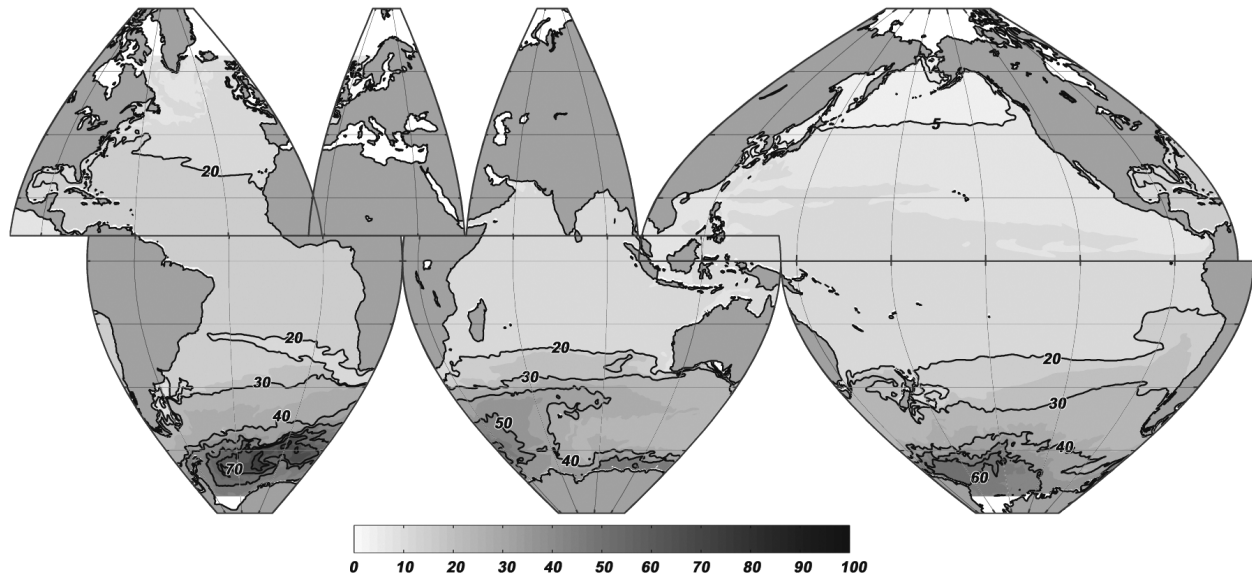


FIG. 16. Global tracer concentration of  $C_{BW}$  (%) at the surface model level after 1000 yr of integration time.

Between the source region and the point of its ultimate separation from the American margin, the DWBC branches a number of times primarily at the depth of the greatest signal. At the equator a tightly constrained signal with  $\sim 1^\circ$  meridional extent, centred at  $\sim \frac{1}{2}^\circ\text{N}$  and with a maximum concentration between 2750 and 3300 m, propagates eastward across the basin in an equatorial jet, branching to the north and south on reaching the African coast. Numerous observations have been made of these jets using hydrographic data to infer geostrophic currents (Zangenberg and Siedler 1998), from direct current measurements using lowered acoustic Doppler profilers (Gouriou et al. 2001, 1999), and from tracer measurements (Andri  et al. 1998). It has been shown that they represent a permanent feature in each of the equatorial oceans. In fact, the structure is more complicated, comprising a number of stacked jets with associated EEJs flowing in the opposite direction. No stacking can be

identified in the POCM simulation because the observed distance between jets ( $\sim 400\text{--}600$  m) is comparable to the vertical model resolution at this depth. Only a single maximum is evident, which is selectively sourced by the DWBC.

To the north of the equator a strong tracer signal breaks away from the coast and recirculates to the northwest, bordered to the east by the MAR. A further branching of this flow takes a majority of the tracer through a gap in the MAR at  $\sim 10^\circ\text{N}$  and northeastward into the central basin. Similar pathways were inferred based on a transatlantic section along  $11^\circ\text{N}$  (Friedrichs and Hall 1993) and on CFC observations (Smethie et al. 2000), which demonstrated the existence of a deep recirculating gyre in the Guiana Basin running parallel to the continental shelf between the equator and  $\sim 20^\circ\text{N}$ . The simulated flow, however, lacks the observed northern return flow of the recirculating gyre, as the majority

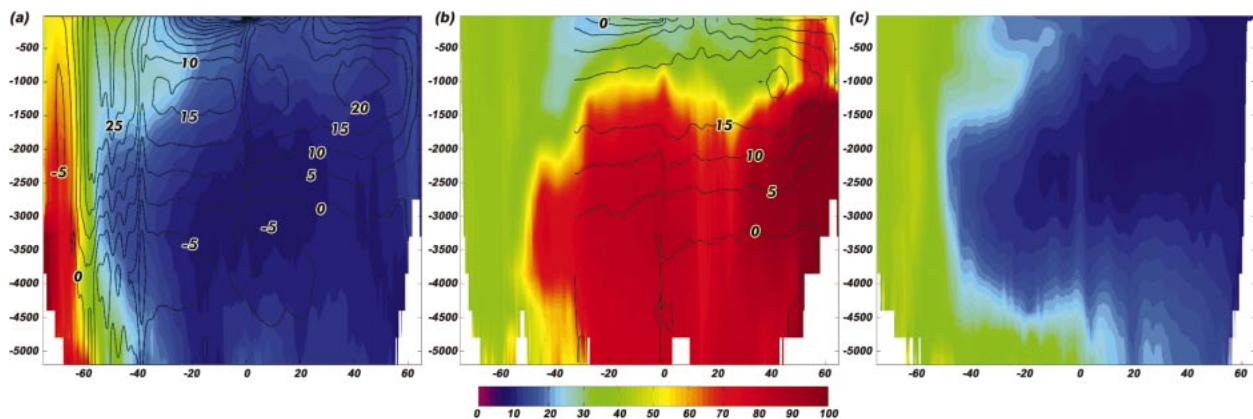


FIG. 17. Zonal mean passive tracer (%) for (a)  $C_{BW}$  global ocean, (b)  $C_{NADW}$  North Atlantic, and (c)  $C_{NADW}$  Pacific Ocean. The meridional overturning streamfunction (Sverdrups) is superimposed (black contours) for the (a) global and (b) North Atlantic regions.

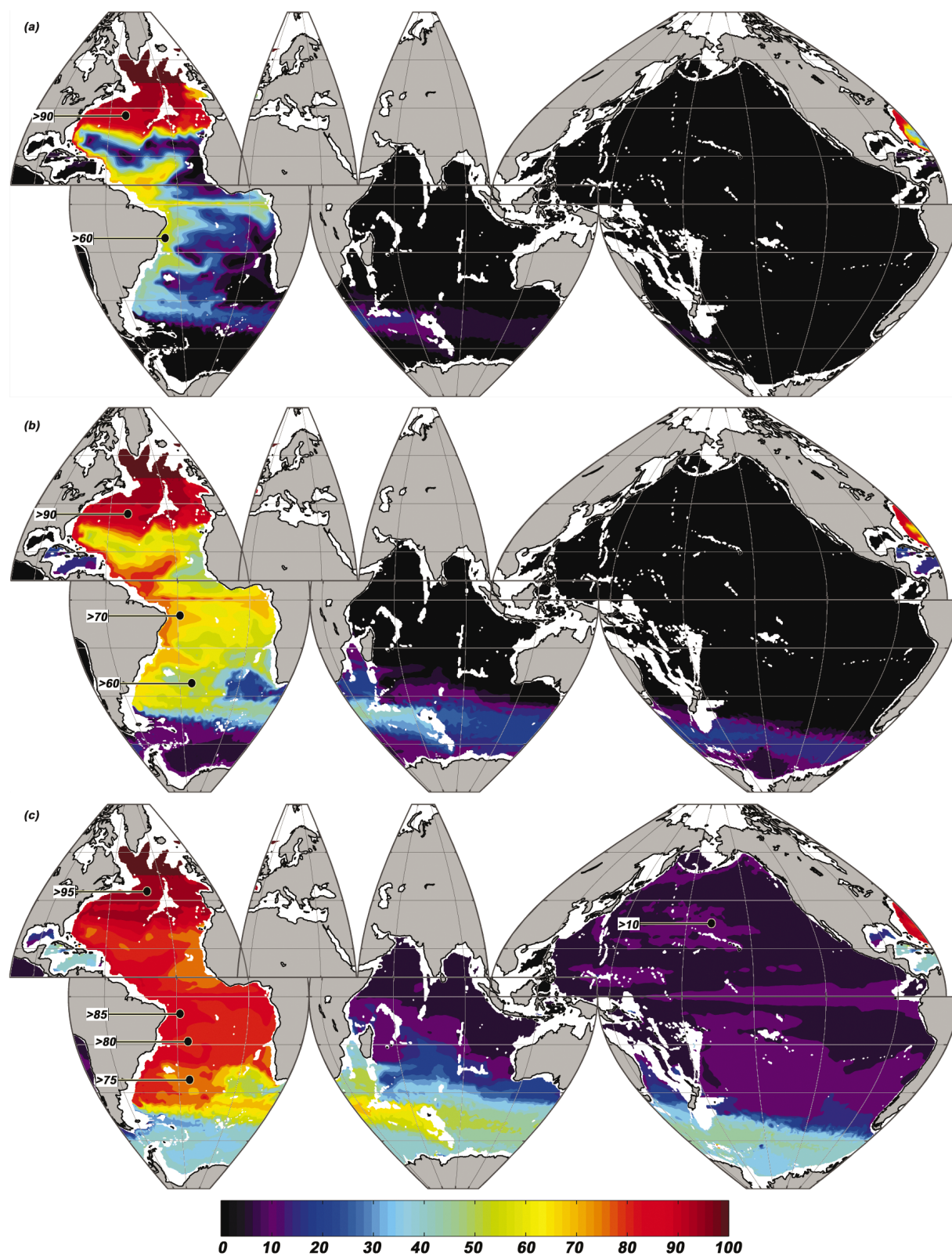


FIG. 18. Concentration of  $C_{\text{NADW}}$  (%) at the depth of greatest NADW outflow, model level 15 (2200–2750 m) (a) after 100 yr of integration, (b) at 300 yr of integration, and (c) at 1000 yr of integration.

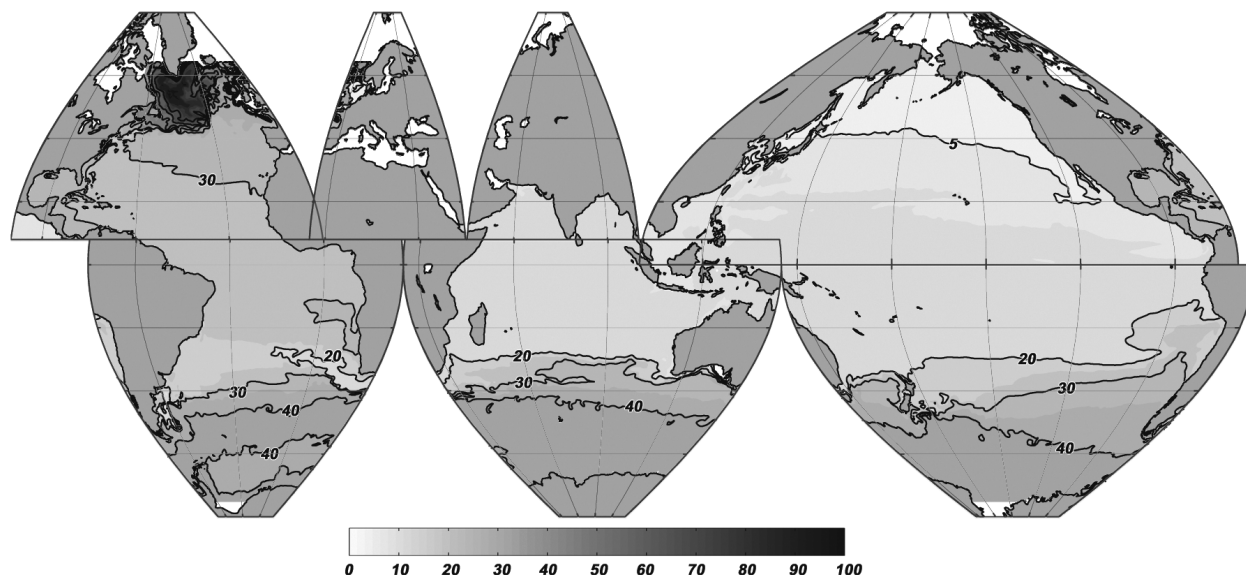


FIG. 19. Global tracer concentration of  $C_{\text{NADW}}$  (%) at the surface model level after 1000 yr of integration time.

of tracer is removed from the western basin through an unrealistically large gap in the MAR. Just south of the equator another offshoot heads southeastward, which at depth is constrained within the Brazil Basin. This feature is in agreement with observations of Larque et al. (1997) who suggest two recirculations of NADW branching off the DWBC; one just below the equator and the other at  $\sim 10^\circ\text{S}$ .

The simulated DWBC branches once again in the vicinity of the Vitorio–Trinidad Ridge, which runs almost perpendicular to the continental margin at  $\sim 20^\circ\text{S}$ . One branch heads southeastward away from the western boundary; at depth this flow is constrained by the MAR while shallower flow extends across the basin to the African margin (from where it continues southward). Zangenberg and Siedler (1998) describe how potential vorticity conservation and local topographic changes lead to this bifurcation.

After a long integration (see Fig. 18c) significant levels of tracer get mixed eastward across the Atlantic basin at mid- and deep levels. At depths shallower than the DWBC core, any upwelled tracer is strongly constrained north of the southern tip of South Africa. Here, entry of tracer-free Indian Ocean origin waters within the Aghulas Current results in a sharp drop in tracer concentrations. The intrusion of “return flow” waters taking the so-called “warm route” from the Indian Ocean (Gordon 1986) in the upper branch of the thermohaline circulation is thus important over a large proportion of the mid to upper water column. Stramma and Siedler (1988) present an analysis of WOCE data that shows input of Indian Ocean waters to depths of at least 1200 m. Below this, but most strongly between 2200 and 2750 m, the DWBC continues southward along the western boundary until it finally separates from the coast north of  $45^\circ\text{S}$  and flows eastward as part of the ACC. During

its eastward transit the depth of maximum tracer shoals from 2200 to 2700 m at the point of separation to between 1300 and 2200 m within Drake Passage, after a complete circuit of Antarctica. This is associated with the large-scale upwelling of NADW and one of its by products, CDW. Idealized age tracer (Stevens and Stevens 1999) and Lagrangian particle (Döös 1995) experiments based on the flow field of the Fine-Resolution Antarctic Model (FRAM) show a similar shoaling.

At the surface, significant levels of resurfacing  $C_{\text{NADW}}$  tracer are only evident south of the Aghulas Current intrusion and extends as a continuous band stretching around the Southern Ocean (Fig. 19). This tracer has been upwelled through deep convective mixing and Ekman divergence in the Southern Ocean, fed by the deep southernmost branch of NADW. Some northward intrusion of NADW into the southern portions of the Indian and Pacific Oceans occurs in the upper levels via the various surface currents (most notably the Humboldt Current). However, even after the 1000-yr integration, surface tracer levels are small. As with the  $C_{\text{BW}}$  experiment there is a significant export of  $C_{\text{NADW}}$  tracer into the Indian and Pacific basins as intermediate water (Fig. 17c). The most significant northward penetration, however, occurs in the deep Pacific basin along pathways common to the lower CDW (see section 4a).

## 5. Discussion and conclusions

We have developed an offline tracer transport model run at an eddy-permitting resolution to investigate interior ventilation pathways on interdecadal to intercentennial timescales. Ventilation on interdecadal time scales is assessed through a comparison between modeled CFC-11 tracer, incorporating a variety of MLD criteria, and observations. Modeled intercentennial ven-



tilation is assessed through comparisons with observed  $\Delta^{14}\text{C}$ . The offline methodology has allowed us to integrate the ventilation experiments for unprecedented lengths of time at eddy-permitting resolutions, providing a cost-effective way to assess interior ventilation in high-resolution simulations.

The use of an eddy-permitting grid significantly improves the fidelity of an ocean model. The lower-resolution OCMIP models (Dutay et al. 2002) showed significant intermodel variability in tracer inventory and penetration depths, with the respective models performing very differently along separate sections. Our offline model performed consistently well over all analyzed sections, capturing most of the observed large-scale ventilation features, apart from the lower NADW core. The improved fidelity was, however, dependent on incorporation of a seasonally varying MLD parameterization that captured open ocean convection during wintertime evaporation and cooling of the surface layer. Without the MLD parameterization, CFC-11 inventories fell far below observations in the areas where convective processes were important. The method of parameterization (Kara et al. 2000) gave a realistic spatial distribution of MLDs (Fig. 1 shows zonally averaged information) with the best agreement in areas of deep penetration. There was poorer representation of the widespread shallow mixed layers, evident particularly in the Southern Hemisphere oceans. This, however, was a consequence of the lack of shallow mixed layers in the original POCM-derived temperature field. Thorpe et al. (2004) note excessively strong density gradients in the surface levels of the POCM.4C simulations, which inhibit these widespread shallow mixed layers. They suggest that this is a result of use of the Pacanowski and Philander (1981) vertical mixing scheme, which was designed primarily for tropical regions and tends to underestimate surface mixing at high latitudes. This problem was mitigated, to some extent, by our use of an increased vertical diffusion coefficient across the uppermost model levels to mimic the wind-driven mixing over the upper 50 m of the ocean. An MLD criterion of  $\Delta T = 0.2^\circ\text{C}$  gave the most realistic mixed layer depth distribution. This is smaller than the optimal criteria calculated by Kara et al. (2000) of  $\Delta T = 0.8^\circ\text{C}$ . A comparison between observed (Levitus et al. 1994) and POCM potential density (not shown) reveals that the modeled isopycnals are often steeper than observed in regions where deep convection is prevalent. This explains why we obtained the most realistic MLD field with the smaller ( $\Delta T = 0.2^\circ\text{C}$ ) criterion. An additional CFC integration performed using the observed MLDs of Kara et al. (2003) produced results very similar to the CFC<sub>0.2</sub> experiment, except for small changes in the depth of penetration of some of the mode waters.

The simulation performs particularly well at capturing thermocline, mode, and surface waters. An analysis of surface CFC-11 concentrations along the various sections (not shown), however, demonstrates that the pa-

rameterization of CFC uptake generally results in some underestimation of modeled surface values at higher concentrations. At greater depths agreement generally becomes poorer. The upper core of NADW is present as a fast-flowing boundary current; however, CFC-11 concentrations are weaker than observed and do not spread far enough from the western boundary. The eastward spread might be expected to be greater if the offline eddy mixing had not been diminished by averaging. However, this does not seem to be the case, because the online eddy-permitting model of Beismann and Redler (2003, their Fig. 5b) shows a CFC-laden boundary current that is equally constrained. Beismann and Redler also compare their eddy-permitting model flow with that of a coarse-resolution model and note that at sub-eddy-permitting resolutions the DWBC becomes overly diffuse and sluggish and a distinct western boundary preference is only evident south of  $\sim 20^\circ\text{N}$ . This is in contrast to the eddy-permitting models that form a tightly constrained, fast-flowing, boundary current that becomes distinct at  $\sim 30^\circ\text{N}$ . Most of the coarse-resolution OCMIP models show an indistinct DWBC with unrealistic spreading of CFC eastward and insufficient southward penetration (Dutay et al. 2002).

The lower NADW core is entirely absent in our simulations as a result of the model domain not encompassing the formation zone of overflow waters, where atmospheric CFC comes into contact with these dense waters. It is noted, in addition, that no distinct lower core can be seen in the POCM velocity fields, despite the northern "sponge" layer restoring model  $T-S$  to observations north of  $58^\circ\text{N}$ . Bottom-water CFC-11 concentrations, although in good qualitative agreement in the region of the Ross and Weddell gyres, are generally too weak and the extensive area of high CFC-11 observed between  $80^\circ$  and  $150^\circ\text{E}$  is entirely missing. The simulation of the formation and subsequent spread of deep and bottom waters in both the North Atlantic and around Antarctica represents a difficult challenge because many processes are involved: air-sea-ice interaction during formation, deep convection or overflow with consequent entrainment of other waters, BBL flows, and deep circulation patterns. The weak formation of AABW is a common problem of many OGCMs that are forced by temperature and salinity climatologies (e.g., Ribbe and Tomczak 1997); these climatologies are generally biased toward summer conditions, when formation is weak or absent. As such, it is not surprising to find that most studies poorly represent these deep flows. Some improvement has been demonstrated when a bottom boundary layer scheme is implemented (Campin and Gosse 1999; Döscher and Beckmann 2000; Nakano and Sugimotohara 2002) in  $z$ -coordinate models. The BBL schemes result in stronger outflow currents and less entrainment. For instance, the incorporation of a BBL scheme in the eddy-permitting model of Beismann and Redler (2003) sufficiently improved overflow processes in order to produce the previously absent lower



core of NADW. Unfortunately, the altered flow characteristics associated with a BBL scheme make it difficult to incorporate into an offline model where the advective fields are not prognostic. It would also distort the assessment of the online model ventilation as new physics would have to be introduced into the offline model.

For the multicentury integrations the inadequacies in representing deep ventilation can be removed by specifying interior source regions for the passive tracer. The comparison of tracer ages within the Pacific showed good qualitative agreement with observed  $\Delta^{14}\text{C}$  age estimates: significant penetration of young bottom water northward along the Kermadec–Tonga Trench system followed by a clockwise spreading into the northern basin, oldest bottom water situated along the northeast basin (Fig. 13), and old water centered in two cores returning southward at middepth (Fig. 15). In many regions, however, the age values were not in agreement. This is not necessarily a failing of the simulation; it may be a consequence of the different effect that mixing has on tracers with different source functions and decay properties (Waugh et al. 2003). The model age field is also not necessarily at steady state. In short, direct comparison between the absolute model age and  $\Delta^{14}\text{C}$  derived advection age is ambiguous; it is more appropriate to simply compare pathways of penetration of young waters in the model and observed estimates.

The coarse resolution of  $\Delta^{14}\text{C}$  measurements prevents identification of detailed ventilation pathways. However, existing hydrographic surveys do provide a broad picture of deep and bottom water ventilation routes. When we study the idealized tracer of deep North Atlantic source water, the simulated southward passage of NADW as a DWBC is primarily as a single diffuse core. The maximum outflow layer is located between the observed double core. The lack of a double core stems in part from our use of an extended source region in the vertical, implying that the boundary current may be fed by a variety of densities, and from poorly represented overflow processes, which entrain excessive surrounding water during the overflow of the deeper core. This is in contrast to the real ocean that sees only two distinct densities (i.e., LSW and Denmark Strait overflow water) spiked with young waters. Apart from this shortcoming, many of the observed bifurcations in the flow are represented, including some of the structure evident in the equatorial region. The pathways that branch off the main flow often extend too far across the Atlantic basin, where in reality these branches tend to recirculate and re-merge with the boundary current. The simulation correctly represents the final separation of the DWBC to join the ACC. In the Southern Ocean, predominantly within the ACC region, mixing with waters from below increases NADW tracer concentrations at depth from where northward penetration occurs in the lower model levels. Alternatively mixing with waters from above and the circumpolar Ekman divergence brings elevated con-

centrations to intermediate and surface levels where northward penetration occurs under the influence of the surface currents.

Detailed bottom-water pathways are generally consistent with observations, with the main deep northward ventilation occurring in the Pacific, primarily as a series of western boundary currents constrained by the bathymetry and with a number of bifurcations to the east. The eastward bifurcations occur through various gaps in the central Pacific basin ridge systems. It should be noted, though, that only a small proportion of the bottom-water tracer actually flows northwards in the abyssal ocean. Instead, it is largely upwelled south of the ACC (Fig. 17a), where some of the tracer then flows northward as part of AAIW. In contrast, most NADW flows out into the Southern Ocean, with only a small fraction fluxed back to the surface (mainly via the mixed layers exchanging deep and surface waters over winter, Fig. 17b). This difference between NADW and AABW is largely due to the “Drake Passage effect” (Toggweiler and Samuels 1995), which dictates that meridional geostrophic flow across the Drake Passage gap is negligible (because zonal pressure gradients cannot develop without land masses). This means AABW sinking off Antarctica can only be replaced by upwelled CDW/NADW/AABW at the Drake Passage gap—not by upper waters to the north of the gap. In contrast, NADW is drawn out of the North Atlantic into the Southern Ocean since there is no substantial surface divergence (and deep upwelling) north of 30°S (apart from that in the equatorial oceans, but this is thought to be weak in NADW content, and dominated moreover by the shallow equatorial overturning cells (Toggweiler and Samuels 1995).

The offline methodology, when implemented with suitable parameterizations to take account of the temporal averaging of the input fields, provides a powerful tool for the investigation of ventilation at high resolution and over long time scales. The primary limitation is the lack of any possible feedback onto the model dynamics, thus making, for example, offline simulations of climate change impossible. The offline model can, however, be an ideal tool for understanding the present-day ocean ventilation. It also provides the only practical means for assessing interior ocean circulation regimes, at multi-century time scales, in models with eddy-permitting resolution.

*Acknowledgments.* We thank Robin Tokmakian for providing the POCM input data used in this study and the APAC Australian national computing facility for computing resources and technical support. We also thank our anonymous reviewers for their helpful comments. This project was supported by the Australian Research Council.

#### REFERENCES

- Andri , C., J. F. TERNON, M. J. MESSIAS, L. MEMERY, and B. BOURL S, 1998: Chlorofluoromethane distributions in the deep equatorial

- Atlantic during January–March 1993. *Deep-Sea Res.*, **45A**, 903–930.
- Arhan, M., K. J. Heywood, and B. A. King, 1999: The deep waters from the Southern Ocean at the entry to the Argentine Basin. *Deep-Sea Res.*, **46B**, 475–499.
- Aumont, O., J. C. Orr, D. Jamous, P. Monfray, O. Marti, and G. Madec, 1998: A degradation approach to accelerate simulations to steady-state in a 3-D tracer transport model of the global ocean. *Climate Dyn.*, **14** (2), 101–116.
- Beckmann, A., and R. Döscher, 1997: A method for improved representation of dense water spreading over topography in geopotential-coordinate models. *J. Phys. Oceanogr.*, **27**, 581–591.
- Beismann, J. O., and R. Redler, 2003: Model simulations of CFC uptake in North Atlantic Deep Water: Effects of parameterizations and grid resolution. *J. Geophys. Res.*, **108**, 3159, doi:10.1029/2001JC001253.
- Bryan, K., 1969: A numerical method for the study of the circulation of the World Ocean. *J. Comput. Phys.*, **4**, 347–376.
- , and L. J. Lewis, 1979: A water mass model of the World Ocean. *J. Geophys. Res.*, **84**, 2503–2517.
- Campin, J. M., and H. Goosse, 1999: A parameterization of dense overflow in large-scale ocean models in z-coordinate. *Tellus*, **51A**, 412–430.
- Castle, R. D., and Coauthors, 1998: Chemical and hydrographic profiles and underway measurements from the eastern North Atlantic during July and August of 1993. NOAA Data Rep. ERL AOML-32 (PB98-131865), 82 pp.
- Cox, M. D., 1984: A primitive equation, three-dimensional model of the ocean. GFDL Ocean Group Tech. Rep. 1, 250 pp.
- Doney, S. C., and J. L. Bullister, 1992: A chlorofluorocarbon section in the eastern North Atlantic. *Deep-Sea Res.*, **39A**, 1857–1883.
- , and M. Hecht, 2002: Antarctic Bottom Water formation and deep-water chlorofluorocarbon distributions in a global ocean climate model. *J. Phys. Oceanogr.*, **32**, 1642–1666.
- Döös, K., 1995: Inter-ocean exchange of water masses. *J. Geophys. Res.*, **100** (C7), 13 499–13 514.
- Döscher, R., and A. Beckmann, 2000: Effects of a bottom boundary layer parameterization in a coarse-resolution model of the North Atlantic Ocean. *J. Atmos. Oceanic Technol.*, **17**, 698–707.
- Dutay, J. C., and Coauthors, 2002: Evaluation of ocean model ventilation with CFC-11: Comparison of 13 global ocean models. *Ocean Modell.*, **4**, 89–120.
- England, M. H., 1995: Using chlorofluorocarbons to assess ocean climate models. *Geophys. Res. Lett.*, **22**, 3051–3054.
- , and H. C. Hirst, 1997: Chlorofluorocarbon uptake in a World Ocean model. Part 2: Sensitivity to surface thermohaline forcing and subsurface mixing parameterisation. *J. Geophys. Res.*, **102**, 15 709–15 731.
- , and S. Rahmstorf, 1999: Sensitivity of ventilation rates and radiocarbon uptake to subsurface mixing parameterization in ocean models. *J. Phys. Oceanogr.*, **29**, 2802–2827.
- , and E. Maier-Reimer, 2001: Using chemical tracers to assess ocean models. *Rev. Geophys.*, **39**, 29–70.
- , V. C. Garçon, and J. F. Minster, 1994: Chlorofluorocarbon uptake in a World Ocean model. Part 1: Sensitivity to the surface gas forcing. *J. Geophys. Res.*, **99**, 25 215–25 233.
- Esbenson, S. K., and Y. Kushnir, 1981: The heat budget of the global ocean: An estimate from surface marine observations. Climate Research Institute, Oregon State University, Tech. Rep. 29, 27 pp.
- Friedrichs, M. A. M., and M. H. Hall, 1993: Deep circulation in the tropical North Atlantic. *J. Mar. Res.*, **51**, 697–922.
- Gordon, A. L., 1986: Inter-ocean exchange of thermocline water. *J. Geophys. Res.*, **91**, 5037–5046.
- Gouriou, T., B. Bourlès, H. Mercier, and R. Chuchla, 1999: Deep jets in the equatorial Atlantic Ocean. *J. Geophys. Res.*, **104** (C9), 21 217–21 226.
- , and Coauthors, 2001: Deep circulation in the equatorial Atlantic Ocean. *Geophys. Res. Lett.*, **28**, 819–822.
- Haine, T. W. N., A. J. Watson, M. I. Liddicoat, and R. R. Dickson, 1998: The flow of Antarctic bottom water to the southwest Indian Ocean estimated using CFCs. *J. Geophys. Res.*, **103** (C12), 27 637–27 653.
- Hall, T. M., T. W. N. Haine, and D. W. Waugh, 2002: Inferring the concentration of anthropogenic carbon in the ocean from tracers. *Global Biogeochem. Cycles*, **16**, 1131, doi:10.1029/2001GB001835.
- Hazell, D., and M. H. England, 2003: Prediction of the fate of radioactive material in the South Pacific Ocean using a global eddy-resolving model. *J. Environ. Radio.*, **65**, 329–355.
- Hirst, A. C., 1999: Determination of water component age in ocean models: Application to the fate of North Atlantic Deep Water. *Ocean Modell.*, **1**, 81–94.
- , S. P. O'Farrell, and H. B. Gordon, 2000: Comparison of a coupled ocean–atmosphere model with and without oceanic eddy-induced advection. Part I: Ocean spinup and control integrations. *J. Climate*, **13**, 139–163.
- Kara, B. A., P. A. Rochford, and E. Hurlburt, 2000: An optimal definition for ocean mixed layer depth. *J. Geophys. Res.*, **105** (C7), 16 803–16 821.
- , —, and —, 2003: Mixed layer depth variability over the global ocean. *J. Geophys. Res.*, **108**, 3079, doi:10.1029/2000JC000736.
- Kawabe, M., S. Fujio, and D. Yanagimoto, 2003: Deep-water circulation at low latitudes in the western North Pacific. *Deep-Sea Res.*, **50A**, 631–656.
- Kawase, M., and J. L. Sarmiento, 1985: Nutrients in the Atlantic thermocline. *J. Geophys. Res.*, **90** (C5), 8961–8979.
- Larque, L., K. Maamaatuaiahutapu, and V. Garçon, 1997: On the intermediate and deep water flows in the South Atlantic Ocean. *J. Geophys. Res.*, **102** (C6), 12 425–12 440.
- Levitus, S., 1982: *Climatological Atlas of the World Ocean*. NOAA Prof. Paper 13, 173 pp. and 17 microfiche.
- , R. Burgett, and T. P. Boyer, 1994: *Salinity*. Vol. 3, *World Ocean Atlas 1994*, NOAA Atlas NESDIS 3, 99 pp.
- Manabe, S., and R. J. Stouffer, 1996: Low-frequency variability of surface air temperature in a 1000-year integration of a coupled ocean–atmosphere–land surface model. *J. Climate*, **9**, 376–393.
- Mantyla, A. W., and J. L. Reid, 1983: Abyssal characteristics of the World Ocean waters. *Deep-Sea Res.*, **30A**, 805–833.
- , and —, 1995: On the origins of deep and bottom waters in the Indian Ocean. *J. Geophys. Res.*, **100** (C2), 2417–2439.
- McClean, J. L., A. J. Semtner, and V. Zlotnicki, 1997: Comparisons of mesoscale variability in the Semtner–Chervin quarter-degree model, the Los Alamos sixth-degree model, and TOPEX/POSEIDON Data. *J. Geophys. Res.*, **102** (C11), 25 203–25 226.
- Nakano, H., and N. Sugimoto, 2002: Effects of bottom boundary layer parameterization on reproducing deep and bottom waters in a World Ocean model. *J. Phys. Oceanogr.*, **32**, 1209–1227.
- Orsi, A. H., G. C. Johnson, and J. L. Bullister, 1999: Circulation, mixing, and production of Antarctic Bottom Water. *Progress in Oceanography*, Vol. 43, Pergamon, 55–109.
- Owens, W. B., and B. A. Warren, 2001: Deep circulation in the north-west corner of the Pacific Ocean. *Deep-Sea Res.*, **40A**, 959–993.
- Pacanowski, R. C., and S. G. H. Philander, 1981: Parameterization of vertical mixing in numerical models of tropical oceans. *J. Phys. Oceanogr.*, **11**, 1443–1451.
- , K. W. Dixon, and A. Rosati, 1991: The Geophysical Fluid Dynamics Laboratory Modular 755 Ocean Model users guide. Geophysical Fluid Dynamics Laboratory Ocean Group Tech. Rep. 2, 46 pp.
- Paillet, J., M. Arhan, and M. S. McCartney, 1998: Spreading of Labrador Sea Water in the eastern North Atlantic. *J. Geophys. Res.*, **103** (C5), 10 223–10 239.
- Peltola, E., and Coauthors, 2001: Chemical and hydrographic measurements on a Climate and Global Change Cruise along 24°N in the Atlantic Ocean WOCE section A5R (repeat) during January–February 1998. NOAA Data Rep. OAR AOML-41, 199 pp.
- Prinn, R. G., and Coauthors, 2000: A history of chemically and radiatively important gases in air deduced from ALE/GAGE/AGE. *J. Geophys. Res.*, **105**, 17 751–17 792.
- Reynolds, R. W., T. M. Smith, D. C. Stokes, and W. Wang, 2001: An

- improved in situ satellite SST analysis for climate. *J. Climate*, **15**, 1609–1624.
- Ribbe, J., and M. Tomczak, 1997: On convection and the formation of Subantarctic Mode Water in the Fine Resolution Antarctic Model—FRAM. *J. Mar. Syst.*, **13**, 137–154.
- Rix, N. H., and J. Willebrand, 1996: Parameterization of mesoscale eddies as inferred from a high-resolution circulation model. *J. Phys. Oceanogr.*, **26**, 2281–2285.
- Roemmich, D., S. Hautala, and D. Rudnick, 1996: Northward abyssal transport through the Samoan Passage and adjacent areas. *J. Geophys. Res.*, **101** (C6), 14 039–14 055.
- Saenko, O. A., A. J. Weaver, and M. H. England, 2003: A region of enhanced northward Antarctic Intermediate Water transport in a coupled climate model. *J. Phys. Oceanogr.*, **33**, 1528–1535.
- Santoso, A., and M. H. England, 2004: Antarctic Intermediate Water Circulation and variability in a coupled climate model. *J. Phys. Oceanogr.*, **34**, 2160–2179.
- Schlosser, P., J. L. Bullister, R. Fine, W. J. Jenkins, R. Key, J. Lupton, W. Roether, and W. M. Smethie Jr., 2001: Transformation and age of water masses. *Ocean Circulation and Climate: Observing and Modelling the Global Ocean*, S. Seidler et al., Eds., International Geophysical Series, Vol. 77, Academic Press, 431–452.
- Semtner, A., and R. Chervin, 1992: Ocean general circulation from a globally eddy-resolving model. *J. Geophys. Res.*, **97**, 5493–5500.
- Smethie, W. M., R. A. Fine, A. Putzka, and E. P. Jones, 2000: Tracing the flow of North Atlantic Deep Water using chlorofluorocarbons. *J. Geophys. Res.*, **105** (C5), 14 297–14 323.
- Stammer, D., R. Tokmakian, A. Semtner, and C. Wunsch, 1996: How well does a quarter-degree global circulation model simulate large-scale observations? *J. Geophys. Res.*, **101**, 25 779–25 811.
- Stevens, I. G., and D. P. Stevens, 1999: Passive tracers in a general circulation model of the Southern Ocean. *Ann. Geophys.*, **17**, 971–982.
- Stramma, L., and G. Siedler, 1988: Seasonal changes in the North Atlantic sub-tropical gyre. *J. Geophys. Res.*, **93**, 8111–8118.
- Suga, T. Y., and K. Hanawa, 1997: Thermostad distribution in the North Pacific subtropical gyre: The subtropical mode water and the central mode water. *J. Phys. Oceanogr.*, **27**, 140–152.
- Thorpe, S., D. Stevens, and K. Heywood, 2004: Comparison of two time-variant forced eddy-permitting global ocean models with hydrography of the Scotia Sea. *Ocean Modell.*, in press.
- Toggweiler, J. R., and B. Samuels, 1995: Effect of Drake Passage on the global thermohaline circulation. *Deep-Sea Res.*, **42A**, 477–500.
- , K. Dixon, and K. Bryan, 1989: Simulations of radiocarbon in a coarse-resolution World Ocean model. Part 1: Steady state prebomb distributions. *J. Geophys. Res.*, **94** (C6), 8217–8242.
- Tokmakian, R., and P. G. Challenor, 1999: On the joint estimation of model and satellite sea surface height anomaly errors. *Ocean Modell.*, **1**, 39–52 and Erratum 119–125.
- Visbeck, M., J. Marshall, T. Haine, and M. Spall, 1997: Specification of eddy transfer coefficients in coarse resolution ocean circulation models. *J. Phys. Oceanogr.*, **27**, 381–402.
- Wanninkhof, R., 1992: Relationship between wind speed and gas exchange over the ocean. *J. Geophys. Res.*, **97** (C5), 7373–7382.
- Warner, M. J., and R. F. Weiss, 1985: Solubilities of chlorofluorocarbons 11 and 12 in water and seawater. *Deep-Sea Res.*, **32A**, 1485–1497.
- , and —, 1992: Chlorofluoromethanes in South Atlantic Antarctic Intermediate Water. *Deep-Sea Res.*, **39A**, 2053–2075.
- , J. L. Bullister, D. P. Wisegarver, R. H. Gammon, and R. F. Weiss, 1996: Basin-wide distributions of chlorofluorocarbons F-11 and F-12 in the North Pacific: 1985–1989. *J. Geophys. Res.*, **101** (C9), 20 525–20 542.
- Waugh, D. W., T. M. Hall, and T. W. N. Haine, 2003: Relationships among tracer ages. *J. Geophys. Res.*, **108**, 3138, doi:10.1029/2002JC001325.
- Whitworth, T., B. A. Warren, W. D. Nowlin Jr., S. B. Rutz, R. D. Pillsbury, and M. I. Moore, 1999: On the deep western-boundary current in the Southwest Pacific Basin. *Progress in Oceanography*, Vol. 43, Pergamon, 1–54.
- Zangenberg, N., and G. Siedler, 1998: Path of the North Atlantic Deep Water in the Brazil Basin. *J. Geophys. Res.*, **103** (C3), 5419–5428.